STRUCTURAL ANALYSIS OF POROSITY EFFECTS ON FRACTURE IN AEROSPACE METAL ADDITIVE MANUFACTURING: A REVIEW

by

JASON T. JOHNSON

MARK E. BARKEY, ADVISOR

A LITERATURE REVIEW AND RESEARCH PROPOSAL

Submitted in partial fulfillment of the requirements
for the degree of Master of Science
in the Department of Aerospace Engineering and Mechanics
in the Graduate School of
The University of Alabama

TUSCALOOSA, ALABAMA

2018

ABSTRACT

Aerospace parts must meet strict structural service and regulatory requirements which is often substantiated by a combination of test and analysis. As the aerospace industry seeks to make metal additive manufacturing as common and reliable as modern subtractive and forming processes, it is necessary to develop methods and design data that enable design engineers to properly size parts in the design phase for the entire part lifecycle. To that end, it is necessary to develop analysis methods to predict the response of structure that contain common defects, such as porosity, that result from the manufacturing process. This paper offers a review of metal additive manufacturing processes commonly used in the aerospace industry, static strength, fatigue, and fracture properties of metal additive manufacturing alloys of interest to aerospace, and common porosity defects that result from the manufacturing process. Additionally, a review of the extended finite element method applied to the study of fracture problems at multiple scales is presented. Next, a relevant case study is presented that studies of the effect porous defects on crack growth. Finally, research that extends from the case study is proposed to further study the effect spherical porosity on crack growth.

CONTENTS

LIST OF TABLES

LIST OF FIGURES

INTRODUCTION

Metal additive manufacturing offers the ability to create near net shape parts which is an attractive benefit to the aerospace industry that can reduce manufacturing time and cost. Aerospace parts must meet strict structural service and regulatory requirements which is often substantiated by a combination of test and analysis. Furthermore, as test costs increase and computational analysis capability increases, lifecycle structural analysis of a part is occurring early in the design process. As the aerospace industry seeks to make metal additive manufacturing as common and reliable as modern subtractive and forming processes, it is necessary to develop methods and design data that enable design engineers to properly size parts in the design phase for the entire part lifecycle. Knowledge of the various additive manufacturing processes, static strength, fatigue, and fracture properties of the materials, as well as the effect of defects is necessary to develop the structural analysis methods and design data required to support this goal.

The literature offers substantial data regarding manufacturing processes and static material properties, however, fatigue and fracture characteristics of aerospace grade alloys, as well as the effect of defects are of high interest in current research. Furthermore, the effect of defects on the fatigue and fracture performance of metal additive manufactured parts is paramount to understand when designing aerospace structure. To that end, it is necessary to develop analysis methods to predict the response of structure that contain common defects, such as porosity, that result from the manufacturing process. This paper offers a review of metal additive manufacturing processes commonly used in the aerospace industry, static strength, fatigue, and fracture properties of metal additive manufacturing alloys of interest to aerospace, and common porosity defects that result from the manufacturing process. Additionally, a review of the extended finite element method applied to the study of fracture problems at multiple scales is presented. The extended finite element method has been shown to be powerful in the modeling of fracture and other discontinuities such as porosity. Next, a relevant case study is presented that studies of the effect porous defects on crack growth. Finally, research that extends from the case study is proposed to further study the effect spherical porosity on crack growth.

METAL ADDITIVE MANUFACTURING IN AEROSPACE

Processes

Several metal additive manufacturing (AM) processes are currently used in the aerospace industry. In order to perform structural analysis required to design aerospace parts that will meet service and regulatory requirements, it is necessary to understand the manufacturing processes involved, the mechanical properties of the materials produced, and the effect of defects on the static strength, fatigue, and fracture properties of those materials. This section reviews the major processes in use, the common types of feedstock used, mechanical properties of common alloys, and finally the porous defects that result from the metal AM process.

Powder Bed Fusion

Powder bed fusion (PBF) processes involve the fusion of thin layers of metallic powder using either a laser or electron beam. A schematic of the PBF process is shown in Figure 1. The selective laser melting (SLM) process projects a laser along a path thereby melting a thin layer of powder. Following the required melting in the build plane, an additional layer of powder is applied and subsequently melted by the laser until the part is completed. The build chamber in SLM is filled with an inert gas, such as argon, to prevent oxidation of the metal during melting. The electron beam melting (EBM) process is similar to SLM except that an electron beam is used to melt the powder. Furthermore, EBM occurs in a vacuum chamber. Both SLM and EBM processes melt only the powder required for the part geometry leaving the remaining powder un-melted. PBF methods result in parts with fine resolution and high quality making them suitable for use in the aerospace industry. However, as a consequence to the detail and quality, PBF processes can be slow and expensive. (Bandyopadhyay & Traxel, 2018; DebRoy et al., 2018; Molaei & Fatemi, 2018; Ngo, Kashani, Imbalzano, Nguyen, & Hui, 2018)

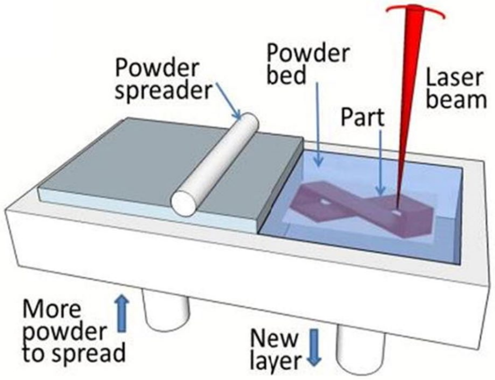

Figure 1: Schematic of powder bed fusion process (DebRoy et al., 2018)

Direct Energy Deposition

Direct energy deposition (DED) is another technique for melting metal powder to manufacture a part. However, DED does not use a bed of powder like PBF. Instead, DED injects the metal powder or wire into the laser beam and deposits the melted metal on a substrate.

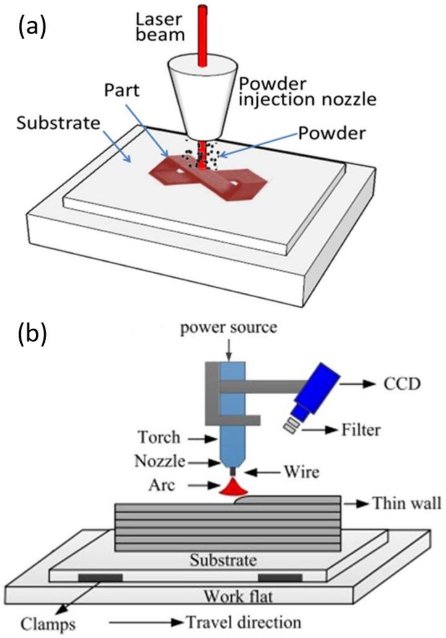

Figure 2: Schematic of direct energy deposition processes process (DebRoy et al., 2018)

Schematics of both wire fed and powder fed DED are shown in Figure 2. DED does not produce as fine detail compared to PBF processes, and typically requires post build machining processes to meet dimensional and surface finish requirements. One major advantage of DED is that it can be used for repairing and retrofitting manufactured parts. (DebRoy et al., 2018)

Table 1: Summary of presented metal AM processes (DebRoy et al., 2018)

Methods	Materials	Applications	Benefits	Drawbacks
Powder bed fusion (SLS, SLM, 3DP)	Compacted fine powders Metals, alloys, and limited polymers (SLS or SLM) ceramic and polymers (3DP)	Biomedical Electronics Aerospace Lightweight structures (lattices) Heat exchangers	Fine resolution High quality	Slow printing Expensive High porosity in the binder method (3DP)
Direct energy deposition	Metals and alloys in the form of powder or wire Ceramics and polymers	Aerospace Retrofitting Repair Cladding Biomedical	Reduced manufacturing time and cost Excellent mechanical properties Controlled microstructure Accurate composition control Excellent for repair and retrofitting	Low accuracy Low surface quality Need for dense support structure Limitations in printing complex shapes with fine details

Metal Alloys and Mechanical Properties

There are several metals used in PBF and DED such as steels, titanium (Ti) and its alloys, nickel alloys, and some aluminum alloys. Ti6Al4V has had extensive study and use in metal AM and is presently used in commercial aerospace and biomedical applications. Only a few aluminum alloys are used such as AlSi10Mg and AlSi12 which are common in casting. Aluminum and its alloys present challenges in AM due to high reflectivity of laser wavelengths used in AM, as well as low viscosity does not allow a large melting pool. Nickel based alloys such as Inconel 625 and 718 are also commonly used in AM. (DebRoy et al., 2018)

For powder based AM processes, fine spherical powders are used because the processes require a high packing density and coordination number to improve consolidation and reduce the number of defects so that high mechanical properties can be achieved. (Romero, Yang, & Bolzoni, 2018) The quality of the powders depends on their manufacturing process. Alloy powders are manufactured using four main processes: gas atomization (GA), rotary atomization (RA), plasma rotating electrode process (PREP), and water atomization (WA). During the GA process, the molten alloy is atomized using a high pressure flow of argon and nitrogen gases. In the RA process, molten metal is poured on a rotary disk and fine droplets or molten metal are flung from the disk. The droplets are solidified and collected. The PREP process is similar to RA in that fine droplets of molten metal are collected as powder, however, PREP creates the droplets in a different manner. During the PREP process, bar stock is melted on one end using an electric arc or plasma. The bar spins about its longitudinal access to eject the molten droplets. Finally, in the WA process, a high pressure water jet atomizes and solidifies molten metal droplets into powder. (DebRoy et al., 2018) Examples of powder shapes produced by each process are shown in Figure 3.

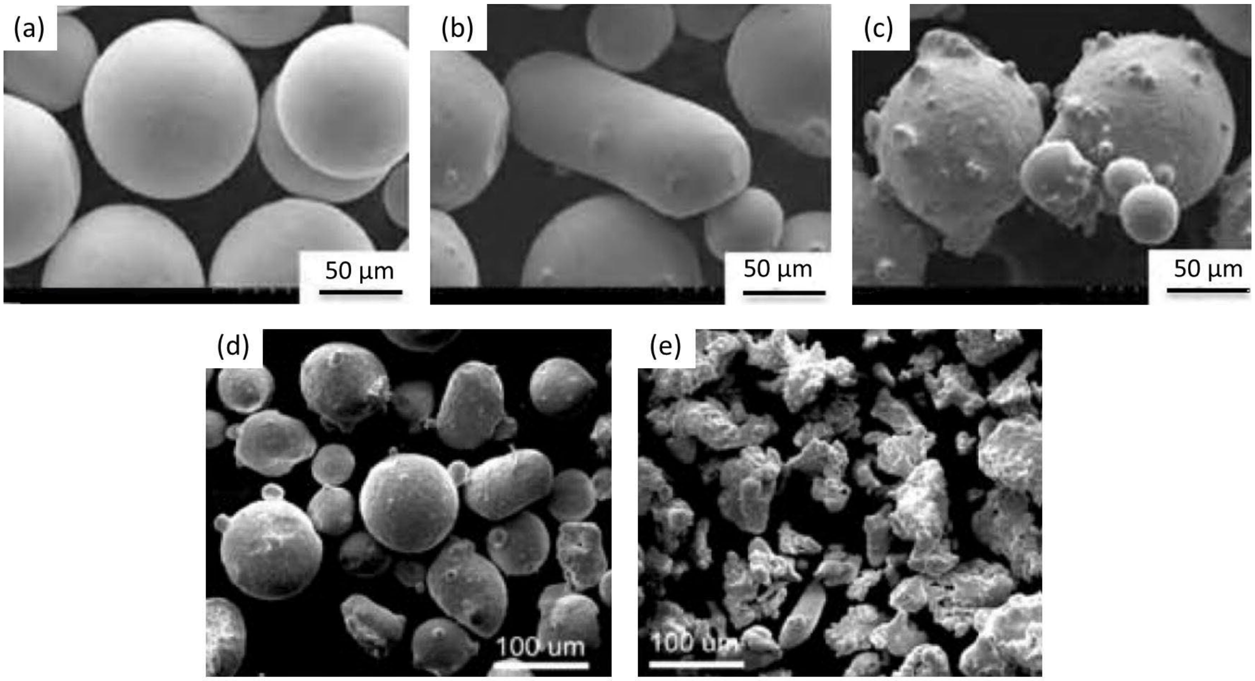

Figure 3: SEM images of alloy powders manufactured by (a) PREP, (b) RA, (c) GA processes, (d) and (e) comparison of powder shapes of GA and WA processes, respectively (DebRoy et al., 2018)

Titanium Alloys

Titanium based alloys are common in aerospace applications, and this high demand has resulted in extensive investigation of these materials. Ti6Al4V is difficult to manufacture using traditional subtractive methods, however AM processes can offer a reduction in manufacturing complexity. Static tensile properties of Ti6Al4V have been thoroughly researched and results for PBF fabricated samples and DED fabricated samples are provided in Table 2 and Table 3, respectively. (Y. Zhang et al., 2018)

Table 2: Mechanical properties of Ti6Al4V fabricated by PBF (Y. Zhang et al., 2018)

Process	Equipment	Condition	Orientation	Young's modulus, GPa	Yield strength, MPa	Ultimate strength, MPa	Failure strain
Wrought	N/A	As fabricated	Longitudinal	113	945	979	0.1
SLM	EOSINT	As fabricated	Horizontal	109	972	1034	0.055
			Vertical	115	1096	1130	0.012
		HIP	Hor. and vert.	112	862	931	0.24

Process	Equipment	Condition	Orientation	Young's modulus, GPa	Yield strength, MPa	Ultimate strength, MPa	Failure strain
	Concept Laser M2	As fabricated	Horizontal	105	1070	1250	0.06
				102	1050	1180	0.08
		HIP	Horizontal	112	1000	1060	0.125
			Vertical	110	920	1000	0.16
	Realizer (SLM300i)	As fabricated	Vertical	119	967	117	0.089
	Trumpf (LF250)	As fabricated	Horizontal	105	1137	1206	0.076
			Vertical	102	962	1166	0.017
		Heat treated	Horizontal	103	944	1036	0.085
			Vertical	98	925	1040	0.075
EBM	Arcam A2	As fabricated	Horizontal	NA	1006	1066	0.15
			Vertical	NA	1001	1073	0.108
	Arcam S12	As fabricated	Horizontal	NA	983	1030	0.122
			Vertical	NA	984	1033	0.09
	Arcam S400	As fabricated	Horizontal	104	844	917	0.088
			Vertical	101	782	842	0.099
		machined	Horizontal	114	899	978	0.095
			Vertical	115	869	928	0.099
	Arcam	As fabricated	N/A	118	830	915	0.131
		HIP	N/A	117	795	870	0.137

Table 3: Mechanical properties of Ti6Al4V fabricated by DED (Y. Zhang et al., 2018)

Feedstock	Process	Material	Condition	Orientation	Young's modulus, GPa	Yield strength, MPa	Ultimate strength, MPa	Failure strain
Powder fed	Wrought	Ti6Al4V	As fabricated	Longitudinal	113	945	979	0.1
	Optomec LENS	Ti6Al4V	As fabricated	Horizontal	116	1066	1111	0.053
					112	832	832	0.008
		HIP		Horizontal	118	949	1006	0.131
				Vertical	114	899	1002	0.118
	Optomec LENS	As fabricated		Vertical	119	908	1038	0.038
		Heat treated		Vertical	118	957	1097	0.034
		Annealed		Vertical	112	959	1049	0.037
	Trumpf DLD	As fabricated		Horizontal	NA	950	1025	0.12

Feedstock	Process	Material	Condition	Orientation	Young's modulus, GPa	Yield strength, MPa	Ultimate strength, MPa	Failure strain
				Vertical	NA	950	1025	0.05
		HIP		Hor. and vert.	NA	850	920	0.17

Zhai et. al. investigated the mechanical properties of Ti6Al4V fabricated by laser engineered net shaping (LENS) and EBM, and characterized microstructure, static properties, and fatigue crack growth mechanisms. LENS is a type of DED process. The resulting as-fabricated room temperature tensile properties are shown in Table 4. The test specimens received post-AM heat treating and resulting mechanical properties are shown in Table 5.

Table 4: Room temperature tensile properties of as-fabricated LENS and EBM Ti6Al4V (Zhai, Galarraga, & Lados, 2016)

	YS (MPa)	UTS (MPa)	el (%)
LENS low power	1005	1103	4
LENS high power	990	1042	7
EBM A2 horizontal	1006	1066	15
EBM A2 vertical	1001	1073	11
EBM Q10 horizontal	973	1032	12
EBM Q10 vertical	1051	1116	15
Mill-annealed	970	1030	16

Table 5: Room temperature tensile properties of heat treated LENS and EBM Ti6Al4V (Zhai et al., 2016)

	YS (MPa)	UTS (MPa)	el (%)
LENS low power	1000	1073	9
LENS high power	991	1044	10
EBM Q10	1039	1294	10

Zhai et. al. observed that as-fabricated LENS and EBM YS and UTS compared to mill-annealed (wrought) forms. The as-fabricated ductility of EBM Ti6Al4V is comparable to the mill-annealed value, but the LENS ductility is lower due to the presence of martensite. The martensite is not present in EBM specimens because of powder bed heating. Heat treatment of the LENS specimens allows for stress relief and reduces martensite resulting in improved ductility. (Zhai et al., 2016)

Additionally, Zhai et. al. investigated fatigue crack growth of LENS and EBM specimens compared to mill-annealed properties. Test specimens were oriented horizontally and vertically relative to build direction as shown in Figure 4. Data for both LENS and EBM in the horizontal and vertical directions, and in both as-fabricated and heat treated conditions are shown in Figure 5.

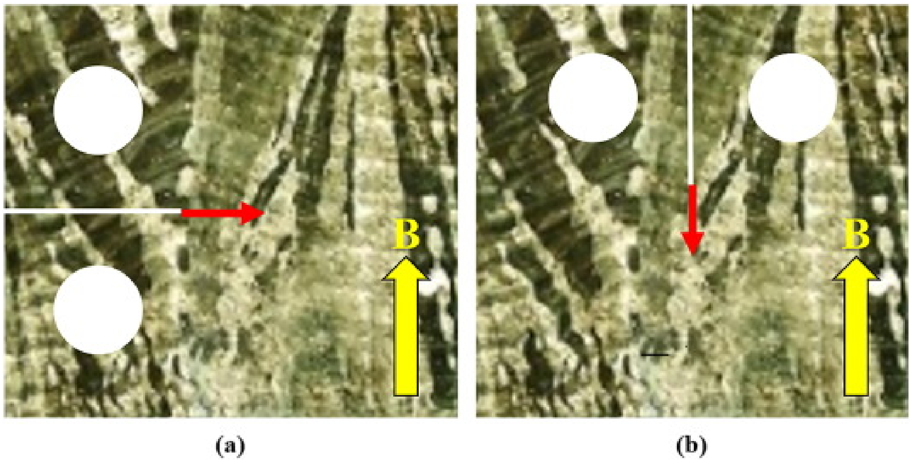

Figure 4: Fatigue crack propagation directions with respect to build direction (B) and columnar grains (a) horizontal and (b) vertical propagation (Zhai et al., 2016)

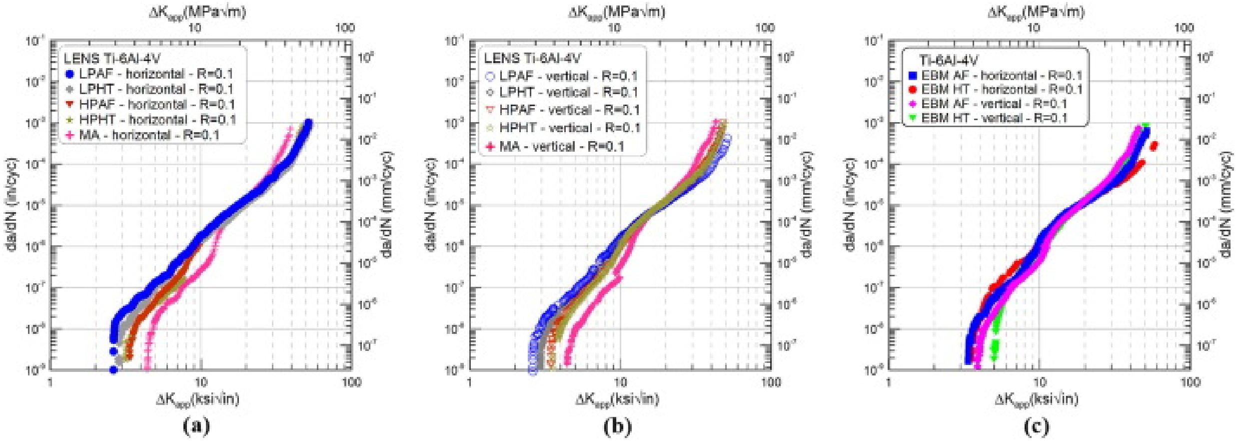

Figure 5: Fatigue crack growth data for LENS Ti-6Al-4V in (a) horizontal and (b) vertical propagation directions, and (c) EBM Ti-6Al-4V, before and after heat treatment (LP – low power, HP – high power, AF – as-fabricated, HT – heat treated) (Zhai et al., 2016)

Aluminum Alloys

Aluminum alloys are a dominant metal in aerospace applications due to their light weight, high strength, and relative low cost. However, aluminum alloys present challenges for use in metal AM. J. Zhang et. al. present the following difficulties in processing aluminum alloys by SLM:

1) Aluminum has poor fluidity which results in agglomeration when spreading the powder which produces uneven thickness of the powder layers and affects layer quality.
2) Laser reflectivity of 91% and high thermal conductivity relative to titanium and ferrous alloys require higher laser powers. Furthermore, lower heat accumulation during forming can result in the formation of defect such as pores and cracks.
3) Aluminum oxidizes easily requiring the removal of oxygen from the processing environment. Oxide films in aluminums induce surface passivation of the molten pool and promote defect formation.

4) High moisture absorption in aluminum powder coupled with extreme differences in hydrogen solubility values of solid versus liquid aluminum results in hydrogen gas porosity when the melted aluminum solidifies rapidly.
5) Aluminum has a high thermal expansion coefficient and a wide solidification temperature range which can generate a large amount of residual stress during rapid solidification producing cracks and part warping.
6) Aluminum alloys contain other metals with low melting points such as magnesium. The fluctuation of alloy composition and crack formation occur easily during laser cycling. (Zhang, Song, Wei, Bourell, & Shi, 2018)

The most commonly used aluminum alloys in AM are AlSi10Mg and AlSi12. (Ngo et al., 2018) J. Zhang et. al. collected mechanical properties for various aluminum-silicon (Al-Si) alloys manufactured by SLM, and the results are presented in Table 6.

Table 6: Mechanical Properties of SLM Al-Si alloys collected from literature (J. Zhang et al., 2018)

Material	Condition	Hardness (HV)	Yield Strength (Mpa)	Ultimate Tensile Strength (Mpa)	Elongation (%)	Reference
AlSi10Mg	As-SLMed	-	270	375	4	See Article for References
	As-SLMed	136	-	396	3.5	
	As-SLMed	139-146	-	360	6	
	As-SLMed	133	322	434	5.3	
	SLM + solution at 450 ◦C	90	196	282	13.4	
	SLM++solution at 550 ◦C	60	90	168	23.7	
	SLM + T6	78	-	187	19.5	
	As-SLMed	125	268	333	1.4	
	SLM + T6	103	239	292	3.9	
	As-SLMed	-	311	391	7.2	
	As-SLMed	-	300	455	5.4	
	As-SLMed	-	255	377	1.2	
	SLM + annealing	-	158	256	9.9	
	SLM + T6	-	210	284	4.9	
AlSi12	SLM+Solution	-	110	190	25	
	As-SLMed	-	260	380	3	

Material	Condition	Hardness (HV)	Yield Strength (Mpa)	Ultimate Tensile Strength (Mpa)	Elongation (%)	Reference
	SLM + annealing	-	95	140	15	
AlSi9Mg	As-SLMed	-	328	379	8.1	
AlSi7Mg0.3	As-SLMed	-	200	400	17-Dec	
AlSiMg0.75	As-SLMed	150	354.9	427.7	2.54	
	SLM + annealing	110	275.4	360.2	4.57	

Domfang Ngnekou et. al. present static and fatigue properties of AlSi10Mg produced by SLM PBF AM. Two build directions were considered (0 and 90 degrees) as well as the effect of T6 heat treatment. The test specimen parameters are shown in Table 7, tensile properties are reported in Table 8, and fatigue S-N curves are shown in Figure 6.

Table 7: Designation of fatigue specimens (Domfang Ngnekou et al., 2019)

Production	Platform temperature (°C)	Post process heating (°C)	Orientation	T6	Desgnation	Ra
P1	150	210	XY	No	P1-XY-MA	/
P2	200	300	XY	No	P2-XY-MA	0.7
				Yes	P2-XY-MA-T6	1.2
			Z	No	P2-Z-MA	1.0
				Yes	P2-Z-MA-T6	1.0

Table 8: Tensile properties and microhardness (Domfang Ngnekou et al., 2019)

Designation	Yield Strength (Mpa)	Rp 0.02 (Mpa)	Ultimate Tensile Strength (Mpa)	Elongation (A) (%)	Hardness (μHV)
P1-XY-MA-T6	/	/	320	1.05	/
	/	/	320	1.1	/
P2-XY-MA	210	172	325	11	136±28
	208	175	330	11	
P2-Z_MA	195	145	350	8	136±24
	195	145	350	8	
P2-XY-MA-T6	275	/	330	14.3	178±53
	285	/	345	15.7	
P2-Z-MA-T6	280	200	300	14.7	180±50
	255	225	330	15.2	
Cast A356-T (See article for reference)	210-300	/	220-330	0.3-4.3	

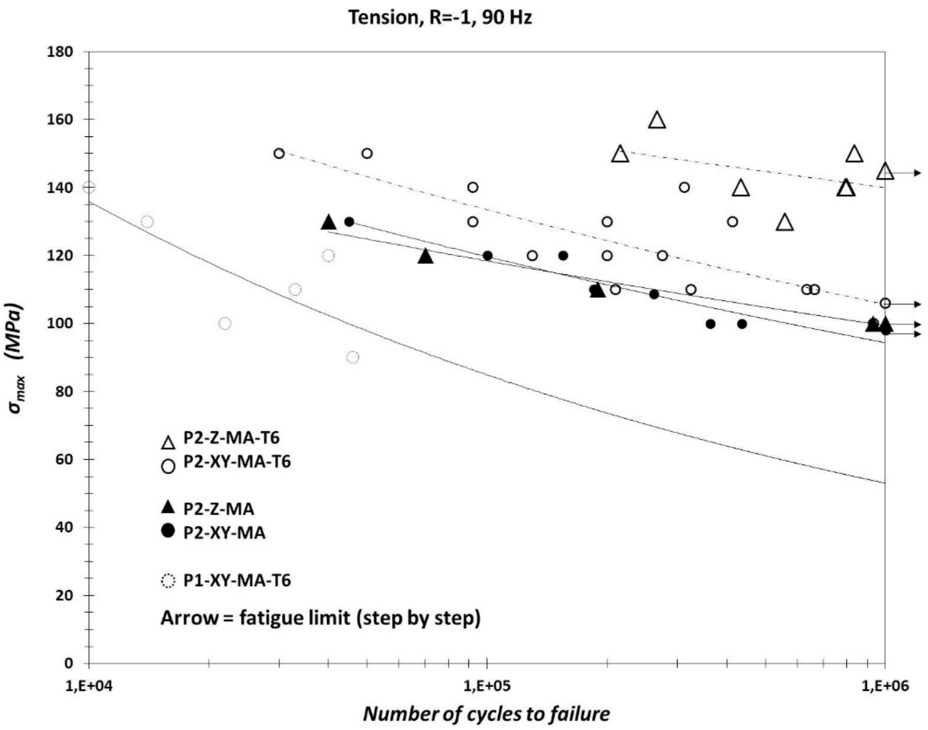

Figure 6: S-N curves for fatigue test specimens (Domfang Ngnekou et al., 2019)

Porous Defects

Porosity is considered a major defect in parts produced by SLM. Two main categories of pores can be considered: metallurgical pores and parameter-based pores. Metallurgical pores originate from absorption of surrounding gasses or from the evaporation of alloying elements such as Mg. Parameter based pores are results of process faults. (Galy, Le Guen, Lacoste, & Arvieu, 2018) The most common cause of fatigue crack initiation in AM parts are generally spherical pores due to entrapped gas, and irregular shaped lack of fusion voids. (Molaei & Fatemi, 2018)

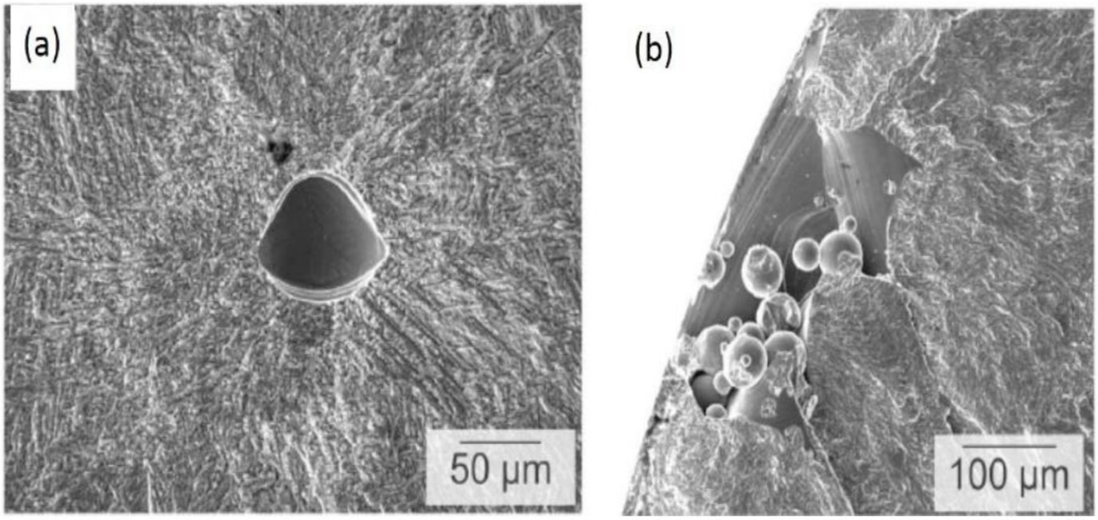

Figure 7: Different typed of defects: (a) nearly spherical pore due to entrapped gas (b) lack of fusion void (Molaei & Fatemi, 2018)

Example images of gas porosity and lack of fusion void are shown Figure 7. The size and shape of the pores affects the performance of the final part. Macro pores are considered more harmful than micro pores, and irregular pore shapes can be the source of cracks. Micro pores can become critical after heat treatment where it has been observed that micro pores can coalesce forming macro pores. (Galy et al., 2018) The effect of pore size on fatigue life of Ti6AL4V samples is shown in Figure 8.

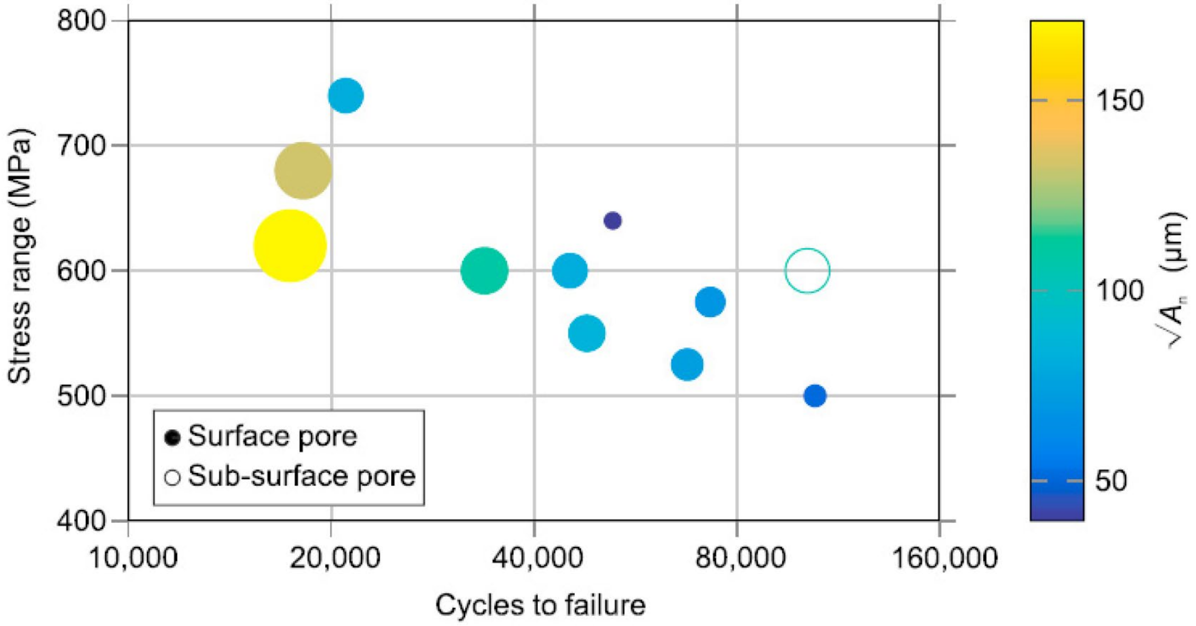

Figure 8: Effect of pore size on fatigue life. The size and color of the markers indicated the size of the pore (A_n) (Molaei & Fatemi, 2018)

The appearance of porosity in aluminum alloys has been related to process parameters, impurities in the feed stock, low laser energy absorption, wettability of solid aluminum by liquid aluminum, atmospheric conditions in the build chamber, and evaporation of elements in the feed stock. (Galy et al., 2018) Galy et. al. produced a porosity root cause tree based on literature review shown in Figure 9.

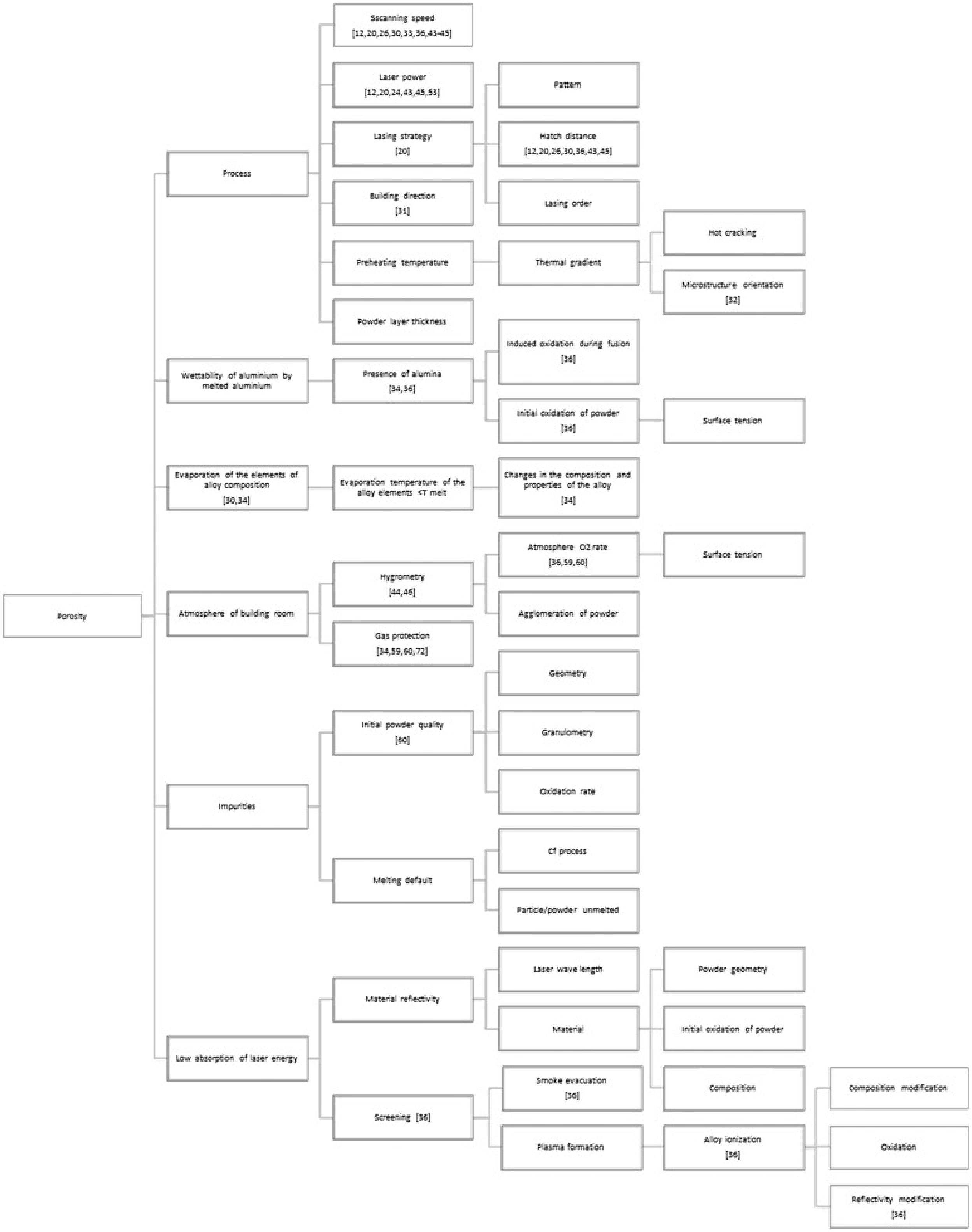

Figure 9: Root causes of porosity (Galy et al., 2018)

For both aluminum alloys and titanium alloys laser scan speed and laser power are recognized as the most influential for porosity level. (Galy et al., 2018) (Molaei & Fatemi, 2018) Figure 8 shows the influence of scan velocity and laser power on the porosity of PBF produced Ti6Al4V samples.

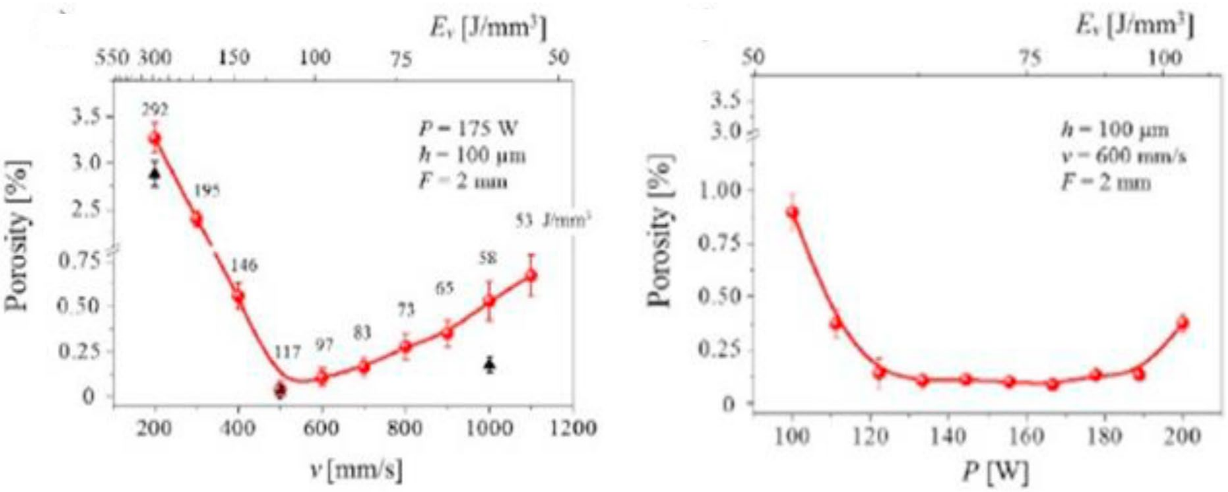

Figure 10: Influence of PBF process parameters on porosity in Ti6AL4V samples: (a) scanning velocity, (b) laser power (Molaei & Fatemi, 2018)

It is interesting to note that porosity increases for relatively slow velocities as well as relatively fast velocities, and relatively low power levels and relatively high-power levels. For low velocities it is possible that the laser over heats the titanium allowing keyhole pores and gas porosities to form, whereas for high velocities, it is possible the laser cannot heat the titanium to high enough temperature resulting in lack of fusion pores. For low power levels it is possible that the laser cannot heat the titanium to high enough temperature resulting in lack of fusion pores, and for high power levels the laser over heat the titanium allowing keyhole pores and gas porosities to form. Keyhole pores are formed at very high power densities and become unstable, repeatedly forming and collapsing leaving voids with entrapped gasses. (DebRoy et al., 2018) An example keyhole pore is shown in Figure 11. Figure 12 shows images of porosity with varying scan velocity and laser power.

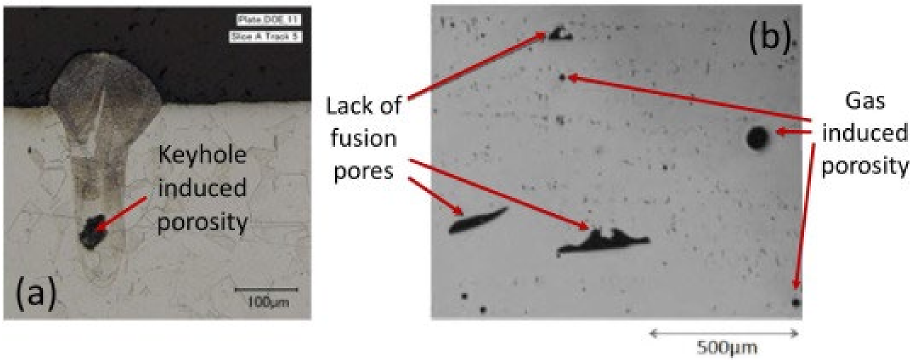

Figure 11: (a) Keyhole porosity, (b) lack of fusion and gas porosity (DebRoy et al., 2018)

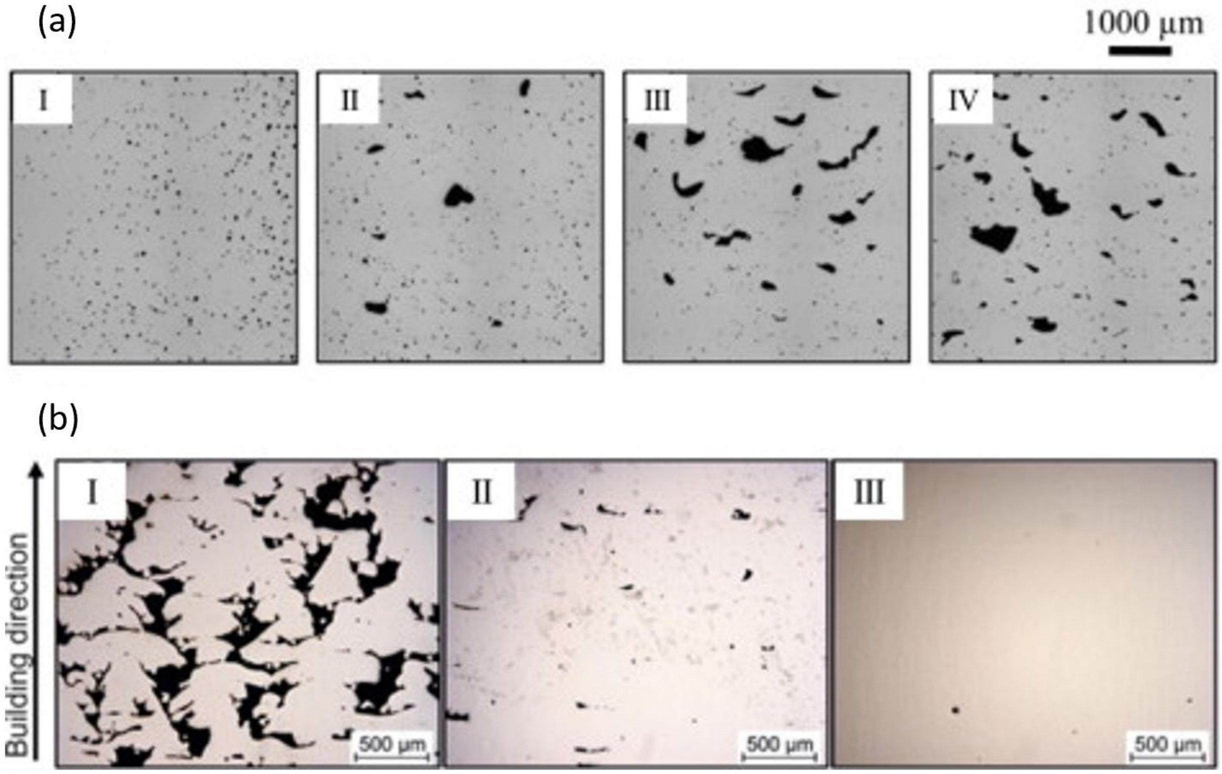

Figure 12: (a) Effect of scanning speed on porosity (I) 250 (II) 500 (III) 750 and (IV) 1000 mm/s, (b) effect of laser power on porosity (I) 90 (II) 120 , and (III) 180 W (DebRoy et al., 2018)

It can be seen from Figure 12 for lower scan velocities spherical gas pores are prominent, whereas for faster velocities irregular shape lack of fusion pores are prominent. Furthermore, for lower laser powers, lack of fusion pores are prominent, and for higher laser powers gas pores are the typical defect. The observations noted from Figure 12 are synonymous with the data shown in Figure 10.

Since pore size, shape, and distribution can vary widely based on process parameters, and have significant impact on fatigue properties, it is necessary to characterize porosity in AM parts. Several techniques exist to measure porosity. The Archimedes method is a simple, non-destructive method to measure porosity for an entire specimen. The volume percentage of porosity is estimated from the density of the component using the Archimedes method. However, the Archimedes method doesn't provide details of the shape, size, or distribution of the pores. Optical microscopy is destructive method to measure porosity that is widely used. 3D porosity of a specimen can only be measured as an area fraction in a particular 2D plane using optical microscopy. As a result, the volume of pores cannot be accurately measured using this technique. Additionally, optical microscopy is not suitable for measuring pores less than 50 µm. X-ray computer tomography (X-ray CT) can measure pores as small as 10 µm and has been used to study porous defects in laser welding. Synchrotron Radiation micro-Tomography (SRµT) can be used to measure formation of porosity. Scanning electron microscopes (SEM), X-ray CT, and SRµT can accurately characterize the shape, size, and distribution of very small pores, but have a high capital equipment cost. (DebRoy et al., 2018) Figure 13 shows pore measurements using the various methods described.

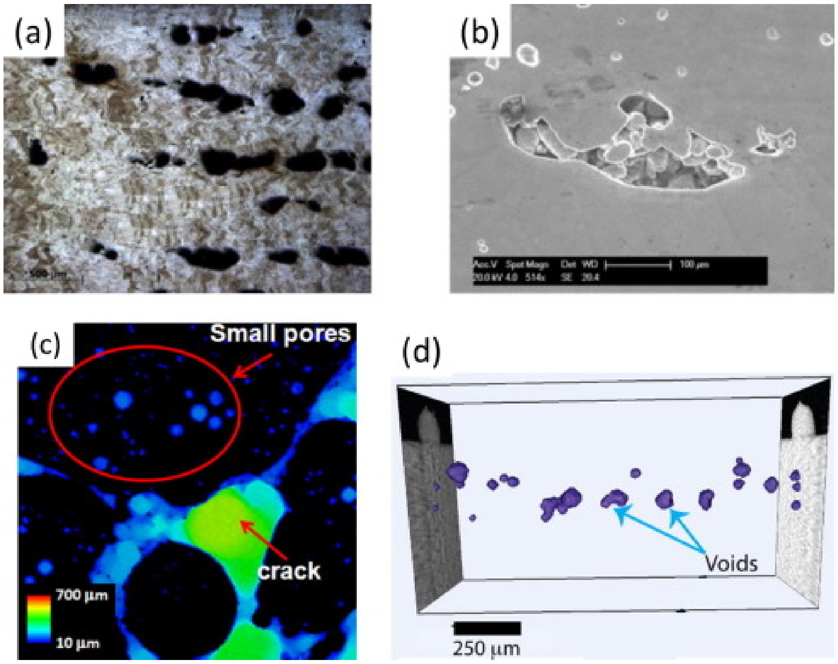

Figure 13: Measurements of porosity and lack of fusion defects using (a) optical microscopy, (b) SEM, (c) X-ray CT, and (d) SRµT (DebRoy et al., 2018)

Seifi et. al. present a defect distribution analysis as part of their work studying parts manufactured using Arcan A2 and A2X machines. Using SEM, X-ray CT they produced spatial location, defect diameter, and other parameters describing defect morphology for the start, middle, and end of the AM build process suggesting that build location can affect porosity. Figure 14 shows defect distribution and characteristics at the start, middle, and end of the build. It is observed from the figure that porosity decreases as build height increases and that defects tend to be located closer to the part perimeter for these particular specimens. Statistical data regarding defect size and area fraction are presented in Figure 15. These figures are representative examples of how defects are characterized in current research. (Seifi, Salem, Satko, Shaffer, & Lewandowski, 2017)

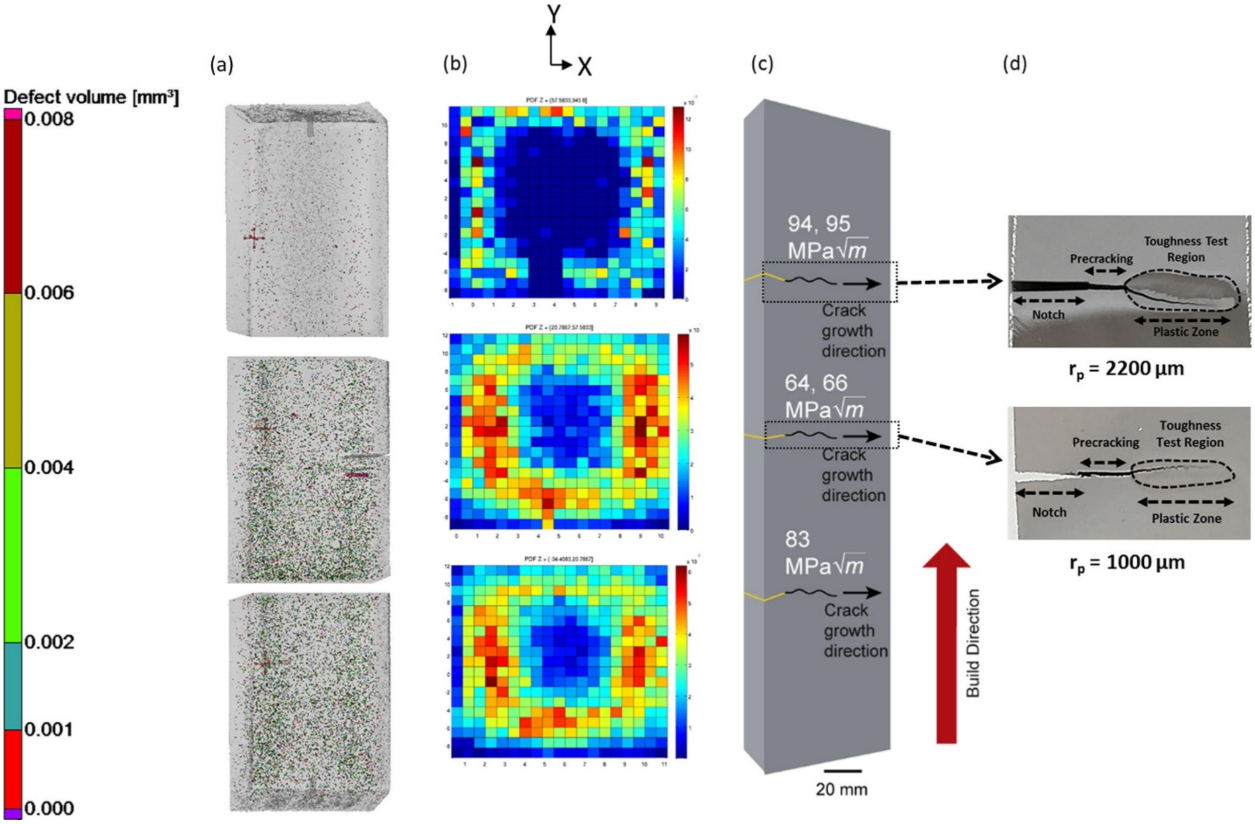

Figure 14: (a) Defect spatial distribution for A2-processed SL sample in as-deposited condition, (b) defect histogram for A2-processed SL sample at start, middle, and end of build, (c) fracture toughness variation throughout the build, (d) extent of plastic zone size at high toughness region and low toughness region (Seifi et al., 2017)

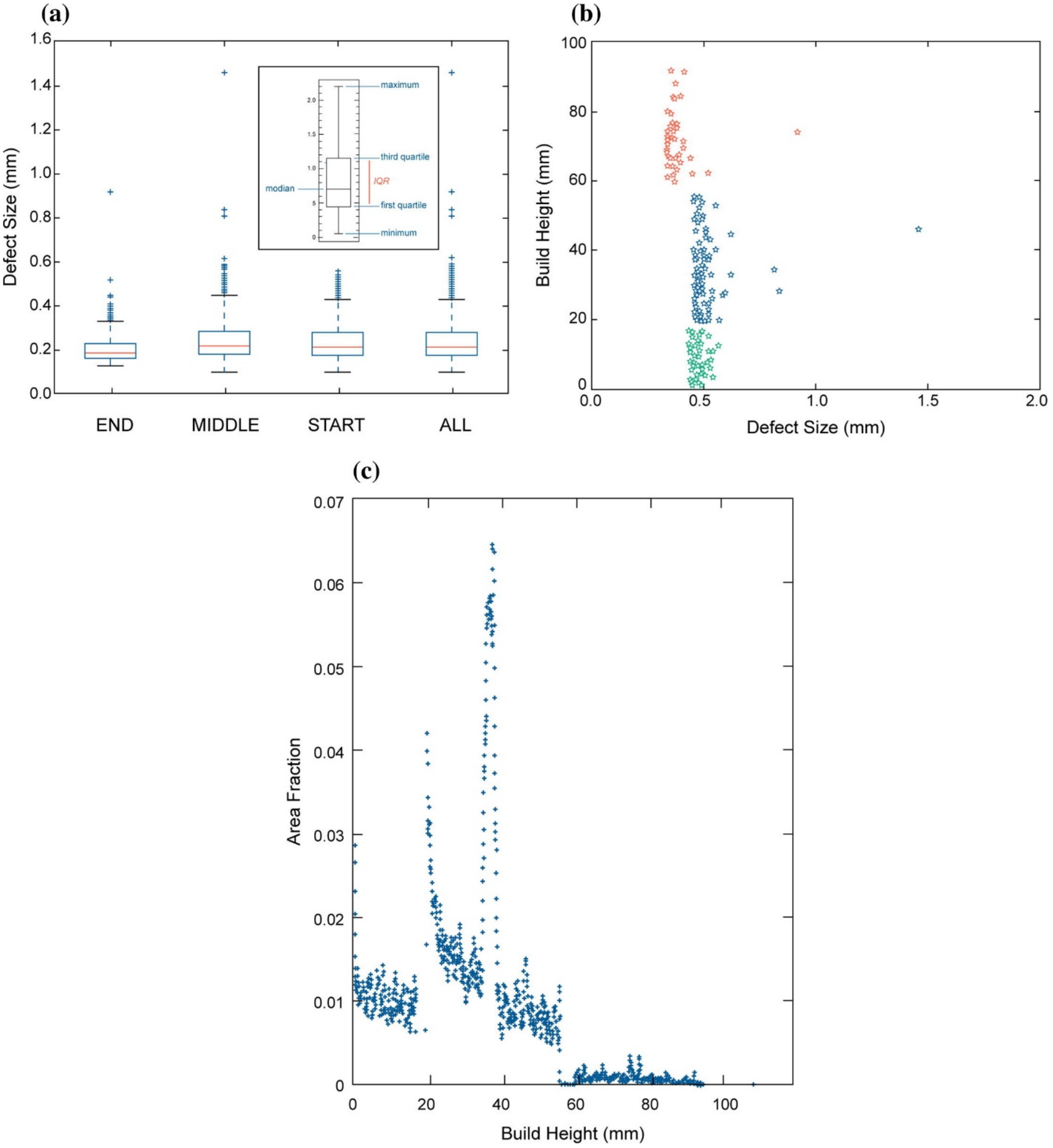

Figure 15: (a) Defect diameter distribution for A2-processed SL as deposited samples at start, middle, and end of build, (b) build height vs. defect diameter for end, middle, and start of A-2 processed SL samples in as-deposited condition, (c) volume fraction of defects vs. build height (Seifi et al., 2017)

EXTENDED FINITE ELEMENT ANALYSIS FOR EFFECTS OF DEFECTS AND FRACTURE

Problems involving discontinuities, singularities, and local deformations such as fracture and porosity can be difficult to analyze using standard finite element methods (FEM). The extended finite element method (XFEM), however, overcomes these difficulties. Discontinuities modeled using XFEM can be categorized into two main types: weak and strong. The most common example of a strong discontinuity is fracture. Weak discontinuities are kinks in the displacement field that result in a jump in strains such as the interface between two different materials. For both strong and weak discontinuities, the standard FEM approach requires mesh topology to conform to the discontinuities. XFEM, however, allows a non-conforming mesh which a great advantage. Figure 16 illustrates an example conforming mesh and non-conforming mesh. XFEM utilizes extrinsic enrichment functions similar to other enriched methods such as partition of unity method (PUM) and the generalized finite element method (GFEM). The partition of unity property states

$$\sum_{\forall I} \varphi_I(X) = 1$$

and all Lagrangian finite element shape functions satisfy it. XFEM exploits the fact that any function $\Psi(x)$ can be reproduced by a product of functions that satisfies partition of unity. The standard FEM approximation can be rewritten then as

$$u^h(X) = \sum_{\forall I} N_I(X)\Psi(X)u_I$$

where N_I are standard FEM shape functions, u_I are nodal degrees of freedom, and $\Psi(X) = 1(X) = 1$. XFEM realizes the possibility of substituting more interesting functions such as discontinuous functions for $\Psi(x)$. This leads to the enriched form

$$u^h(X) = \sum_{\forall I} N_I(X)1(X)u_I + \sum_{\forall I} \varphi_I(X)\Psi(X)q_I$$

where the first summation is the standard FEM approximation and the second summation is the product of unity enrichment, where the nodal values q_I are unknown parameters that adjust the enrichment to best approximate the proposed model. (Belytschko, Liu, Moran, & Elkhodary, 2014)

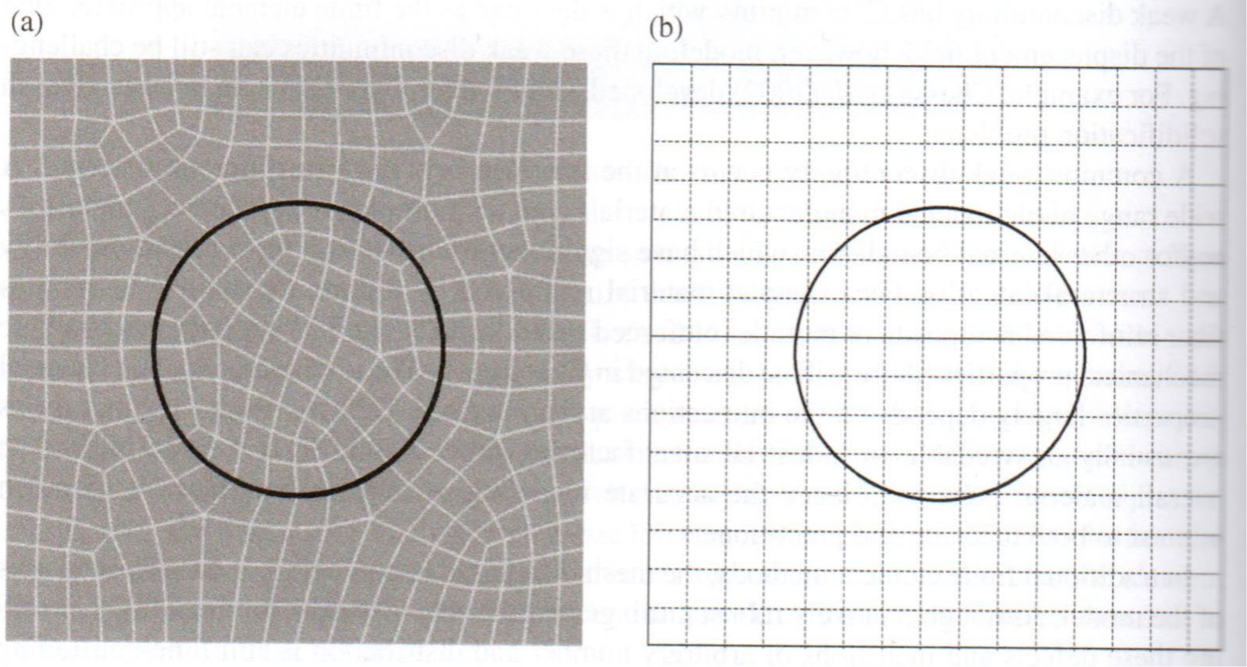

Figure 16: (a) Conforming mesh, (b) non-conforming mesh (Belytschko et al., 2014)

XFEM Applied to Fracture Mechanics

Linear elastic fracture mechanics (LEFM) problems can be solved using XFEM. Consider a 2D crack problem as shown in Figure 17, where the set of nodes in the problem is S_M. The displacement approximation takes the form

$$u^h(X) = \sum_{I\in S_M} N_I(X)a_I + \sum_{I\in S_N} N_I(X)H(X)b_I + \sum_{I\in S_K}\left[N_I(X)\sum_{\alpha=I}^{4} F_\alpha(X)\, c_I^\alpha\right]$$

where N_I are the standard FEM element shape functions, a_I are standard FEM nodal displacements, S_N is the node set of elements where the crack has split the element, b_I are enriched nodal displacements for S_N, S_K is the node set of the element containing the crack tip, and c_i are the enriched nodal displacement for S_K.

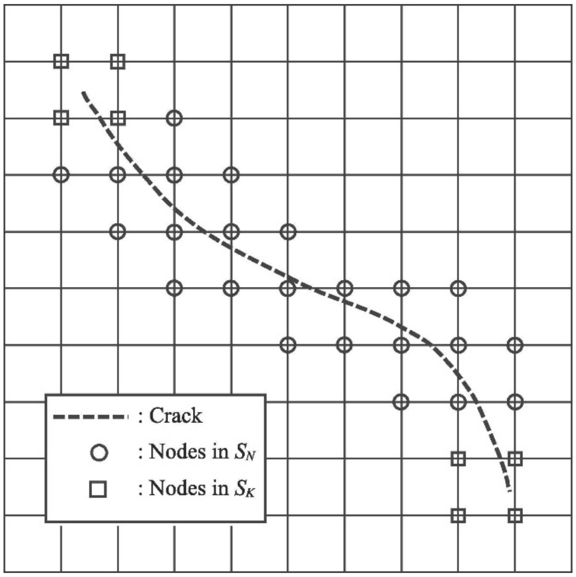

Figure 17: 2D crack problem enriched nodes (Li, Li, & Yuan, 2018)

The Heavyside function, $H(X)$, equals 1 on one side of the crack, and equals -1 on the other side of the crack. The elastic crack-tip branch functions, $F_\alpha(X)$, are based on the description of the displacement fields for the mode I and mode II cracks. (Li et al., 2018)

The XFEM applied to the cohesive zone model results in the displacement approximation in the form

$$u^h(X) = \sum_{I\in S_M} N_I(X)a_I + \sum_{I\in S_N} N_I(X)H(X)b_I$$

where the Heavyside function is posed as

$$H(X) = \begin{Bmatrix} 1, X \in \Omega^+ \\ 0, X \in \Omega^- \end{Bmatrix}$$

The regions Ω^+ and Ω^- are sides of the boundary Γ_c as shown in Figure 18.

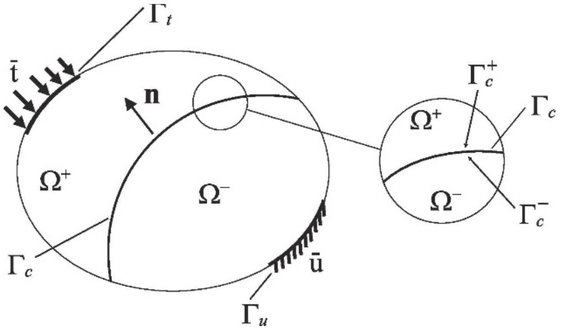

Figure 18: Body Ω *with internal* Γ_c *boundary subjected to loads (Li et al., 2018)*

Since the model assumes that the crack splits an entire element and that the crack tip advances element by element, the crack tip branch functions are neglected. (Li et al., 2018)

XFEM Applied to Multiscale Problems

XFEM can be used to solve multiscale problems involving cracks and other discontinuities. For example, a zoom technique uses a refined mesh for local regions containing stress concentrations. Consider the solid domain Ω shown in Figure 19.

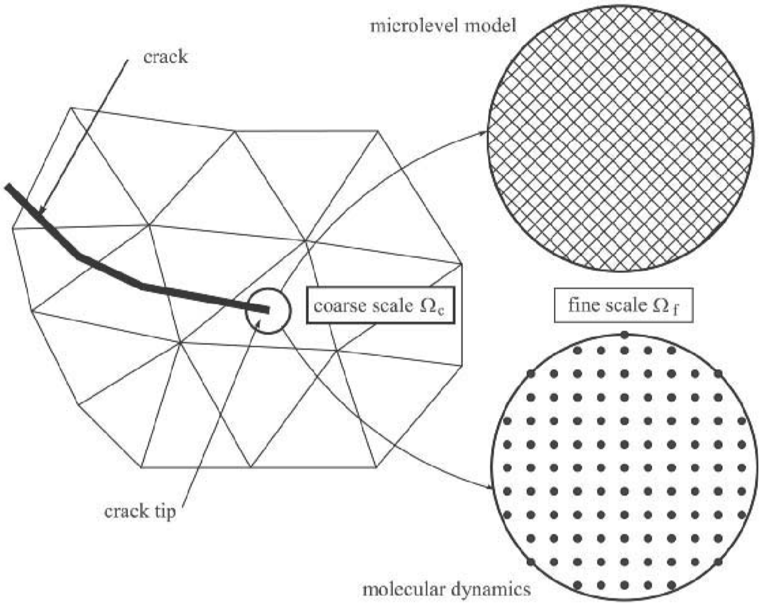

Figure 19: Illustration of example multiscale problem (Mohammadi, 2008)

The domain is split into a coarse meshed, linear elastic portion, Ω_c, and a fine meshed, nonlinear portion, Ω_f, with an interface Γ_{int}. Using a superposition multiscale approach the problem is modeled in global and local parts, and then superimposed to determine the final solution by satisfying the compatibility equations. Another potential method is the multiscale expansion technique based on homogenization of field variables at each scale. Homogenization techniques introduce a displacement discontinuity at the fine scale, therefore, keeping the global coarse scale solution unchanged. An important feature of homogenization based methods is that any fine scale solution can be completely described by the coarse scale. Furthermore, if the microstructure is periodic, then a homogenization procedure can be based on a single unit cell. The partition of unity concept has also been directly applied to multiscale analyses. Using this concept, enrichment functions are applied at multiple scales using partition of unity. Finally, domain decomposition techniques can be used such that the global domain is divided into several other domains connected by interface elements. (Mohammadi, 2008)

Loehnert & Belytschko presented a multiscale projected method using XFEM for macro and microcrack simulations. The method uses a multiscale decomposition of the displacements and projects to the coarse scale using coarse scale test functions. The separation of the problems by scale allows the microscale problem to be solved separately from the macroscale problem providing a substantial savings in computational cost. (Loehnert & Belytschko, 2007) Liu et. al. use the multiscale projection method in their analysis of micro cracks interacting with macro cracks. Their work is presented in this paper as a case study.

Kuman et. al. propose a homogenization scheme to develop effective properties for coarse mesh elements containing microcracks, voids, and inclusions as illustrated in Figure 20. The principle of energy equivalence is used to obtain mechanical properties of the equivalent material. The strain energy density (SED) of the heterogenous material under particular loads and boundary conditions must be equal to the SED of the equivalent homogenous material under the same loads and boundary conditions.

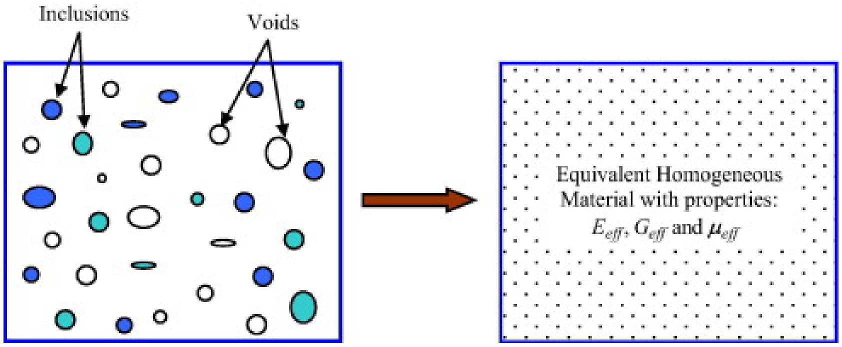

Figure 20: Homogenization of microdefects to equivalent homogenous material properties (Kumar, Singh, & Mishra, 2015)

The homogenized material properties are used in coarse mesh regions of edge cracked plate models as shown in Figure 21. The use of homogenized elements in the far field region of the model shows a significant reduction in computational time compared to discretely modeling the defects throughout the plate. (Kumar et al., 2015)

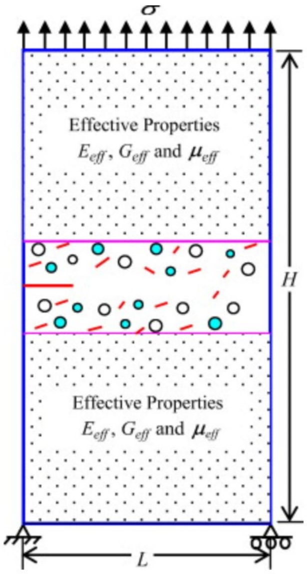

Figure 21: Edge cracked plate with homogenized properties (Kumar et al., 2015)

CASE STUDY

Liu et. al present the results of XFEM simulation of macro scale fatigue crack propagation interacting with micro-defects such as micro-cracks and micro-pores. The multiscale projection method is utilized to study a static crack in the presence of randomly distributed micro-cracks and a growing macro crack in the presence a nearby micro-crack and micro-pore. The growing crack cases are considered separately such that one case is a macro crack in the presence of a micro-crack, and another case is a macro crack in the presence of a micro-pore. The multiscale projection method is utilized here such that the multiscale problem can be separated into two parts: a macro scale model and a micro scale model where the influence of each scale is resolved at the domain boundaries.

The case study considers a two-dimensional (2D) system divided into two domains based on scale. The entire domain under consideration is denoted as Ω^0 with boundary $\partial\Omega^0$. The micro-scale domain around the macro crack tip is denoted as Ω^1 with boundary $\partial\Omega^1$. The micro-scale domain contains the explicit geometry of the micro-defects. Figure 1 depicts the computational domain and micro-scale domain with micro-defects present near the macro crack-tip.

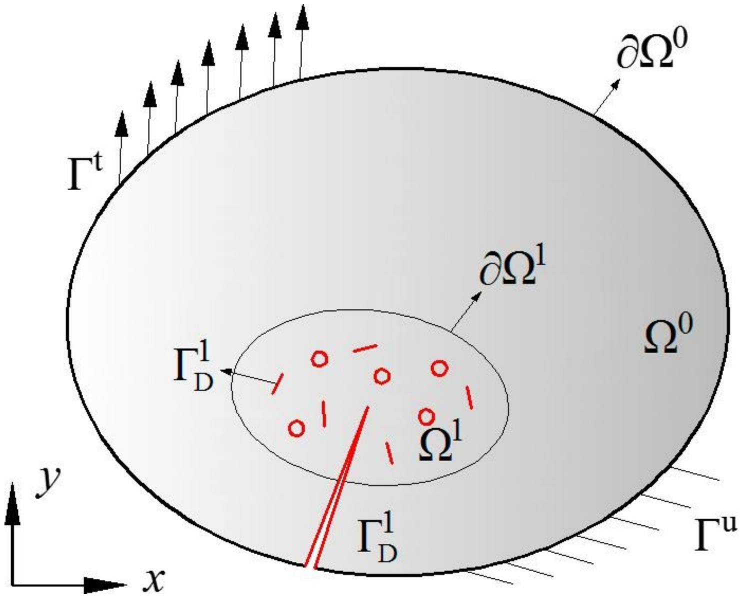

Figure 22: Multiscale computational domain (Liu et al., 2018)

The discretized finite element domain is divided similarly as shown in Figure 2. The domain Ω^0 is meshed using macro scale elements (coarse mesh) and the macro scale elements in the subdomain Ω^1 are subdivided into a refined mesh of micro scale elements (fine mesh).

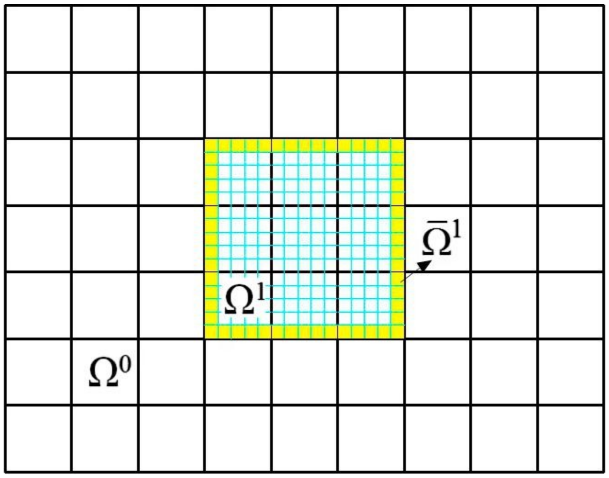

Figure 23: Sketch of coarse scale and fine scale meshes (Liu et al., 2018)

The coarse and fine meshes are used separately such that the coarse mesh is used in the solution of the macro scale problem and the fine mesh is used in the solution of the micro scale problem. The micro defects are only modeled in the fine mesh domain. The multiscale projection method allows the passing of field variables between the two scales while satisfying the required continuity condition along the boundary $\partial\Omega^1$: $u^0 = u^1$.

The multiscale projection method utilized in the case study results in an iterative procedure such that the macro scale problem is solved, the macro scale displacements along the boundary $\partial\Omega^1$ are projected on to the micro scale model, the micro scale model is solved, and an error is calculated. If the error is greater than a prescribed tolerance, then internal forces are calculated for the macro scale model with the influence of the micro scale results. The macro scale model is solved using the new internal forces and the iteration loop continues. A flowchart of the multiscale projection method procedure used in the case study is shown in Figure 3.

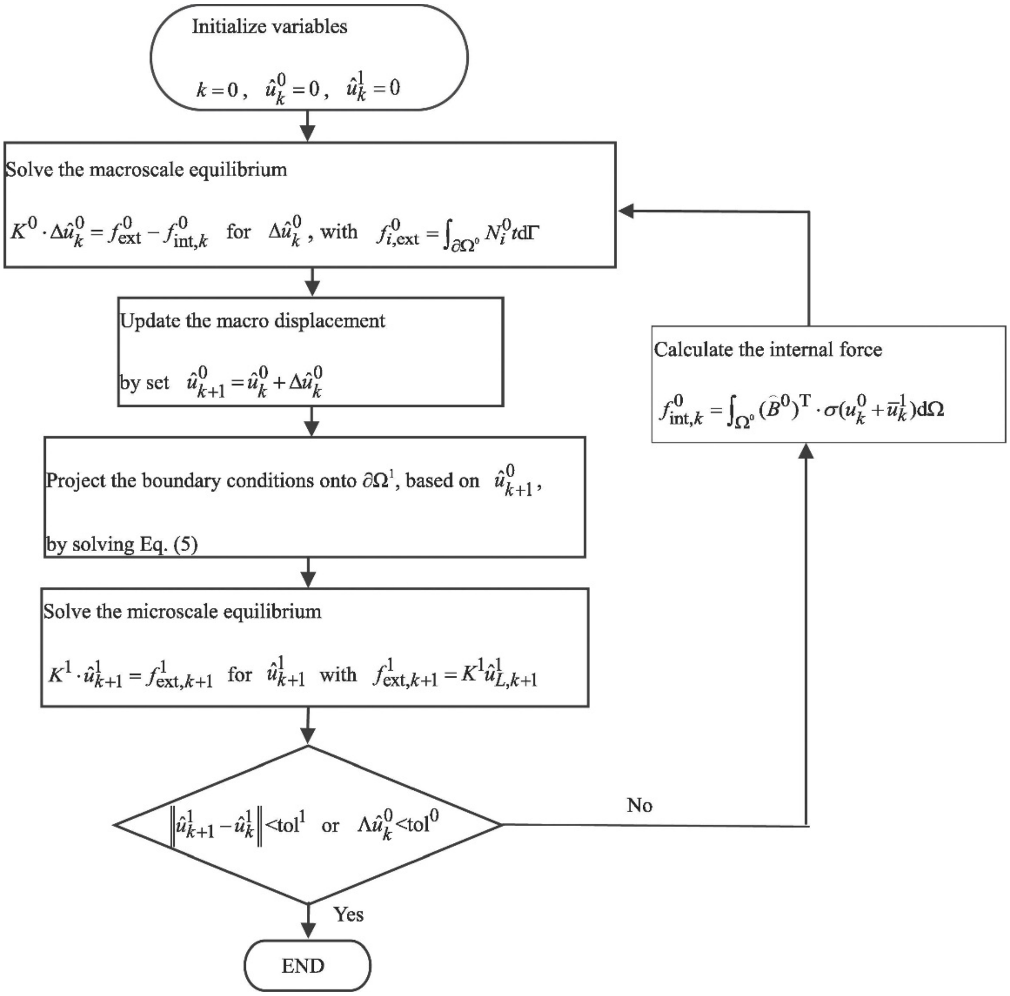

Figure 24: Case study flowchart for multiscale projection method (Liu et al., 2018)

The numerical simulations considered in the case study were chosen to investigate the relationship between micro-defect geometry and its effect on macro crack propagation. The case study first examines how multiple, randomly distributed micro cracks effect the stress intensity factor (SIF) of a static macro crack. Next, a growing macro crack in the presence of deliberately positioned micro-defects is studied. Prior to executing these studies, however, a crack shielding problem is considered to determine the effect of mesh density on simulations of this nature. The mesh density of both the coarse mesh and fine mesh are considered. The crack shielding problem posed considers two micro cracks placed parallel to the macro crack tip as shown in Figure 4.

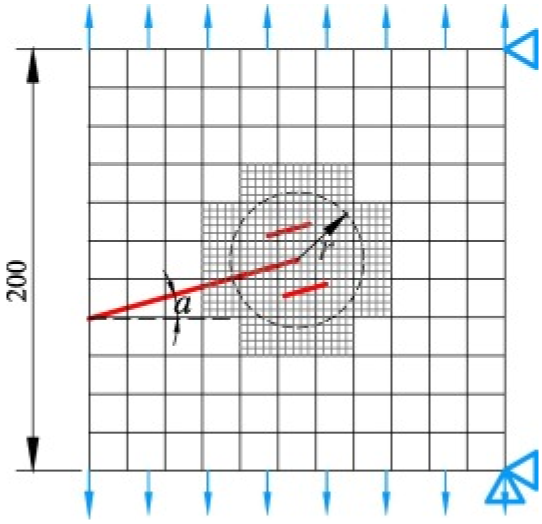

Figure 25: Crack shielding problem (Liu et al., 2018)

The influence of the macro scale mesh density on the micro scale problem is determined by increasing coarse mesh density while holding fine mesh density constant. Similarly, the influence of micro mesh density on the macro scale problem is determined by increasing fine mesh density while holding coarse mech density constant. Normalized SIF are calculated where SIF of the macro crack in the absence of micro cracks is 1.0.

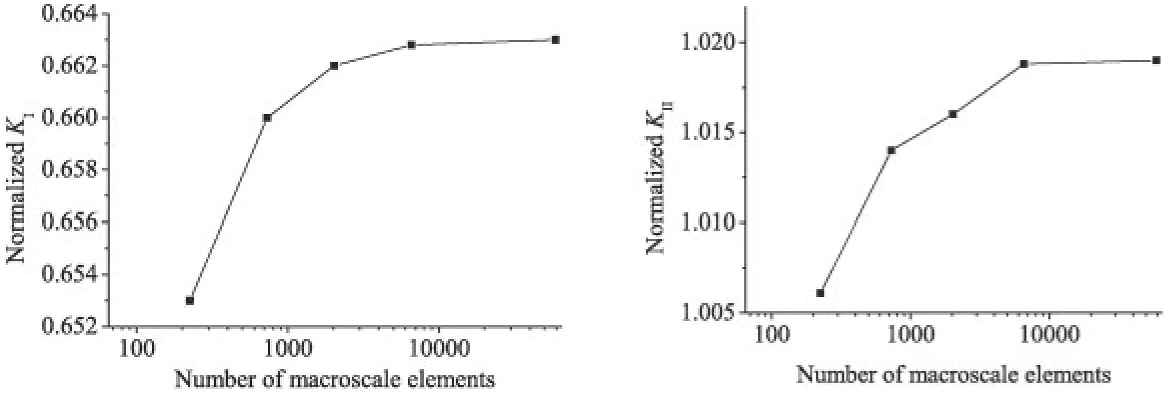

(a) K_I

(b) K_{II}

Figure 26: Normalized SIF results for macro scale mesh density study (Liu et al., 2018)

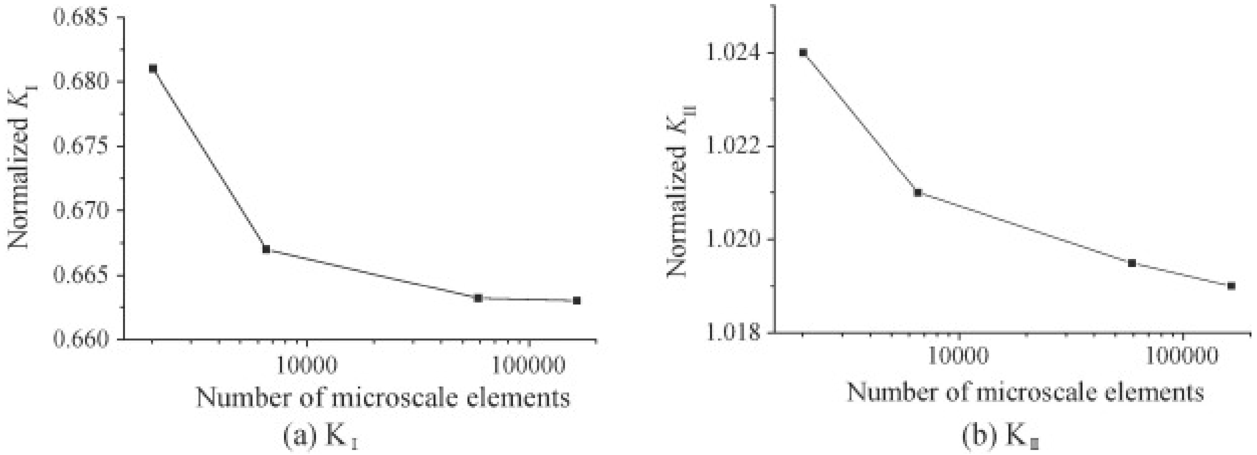

(a) K_I (b) K_{II}

Figure 27:Normalized SIF results for micro scale mesh density study (Liu et al., 2018)

The normalized SIF calculated during the mesh density study are presented in Figure 5 and Figure 6. The case study concludes that mesh density at neither the macro scale nor the micro scale has a considerable effect on numerical results. Although, it is noted that the mesh density of the micro scale mesh influences results more than mesh density of the macro scale mesh, but even a coarse micro scale mesh produced acceptable results.

The case study next considers multiple randomly distributed micro cracks near a static macro crack tip to determine the influence of the micro crack distance from the macro crack tip.

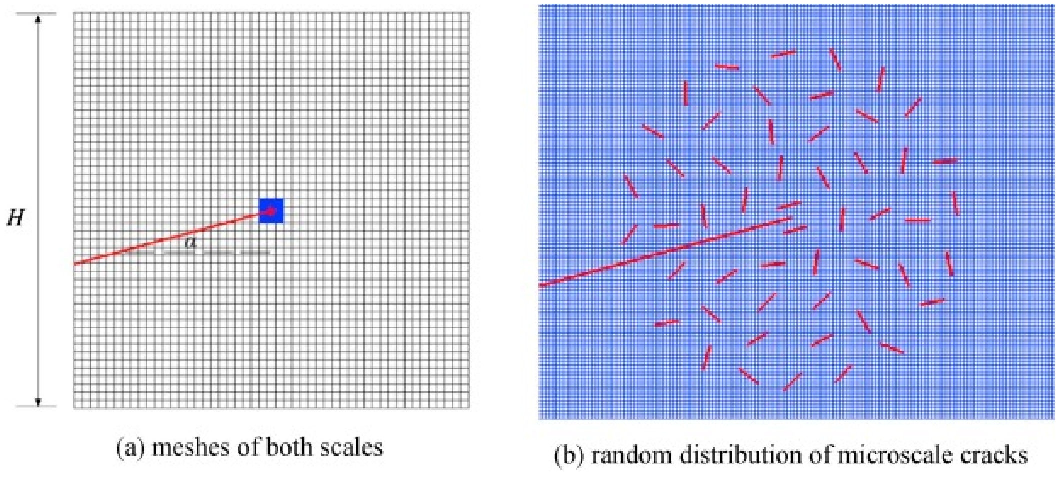

(a) meshes of both scales (b) random distribution of microscale cracks

Figure 28: Sketch of random micro crack distribution (Liu et al., 2018)

The random crack distribution is shown in Figure 7. Fifty micro cracks of equal length are distributed near the macro crack tip with the nearest micro cracks fixed symmetrically and parallel to the macro crack tip. Twenty numerical tests with different micro crack distributions were considered. Furthermore, cases with and without the parallel micro cracks were considered. SIF were calculated for each test. The case study concluded that 95% of the effect on SIF is associated with the nearest microcracks to the macro crack tip.

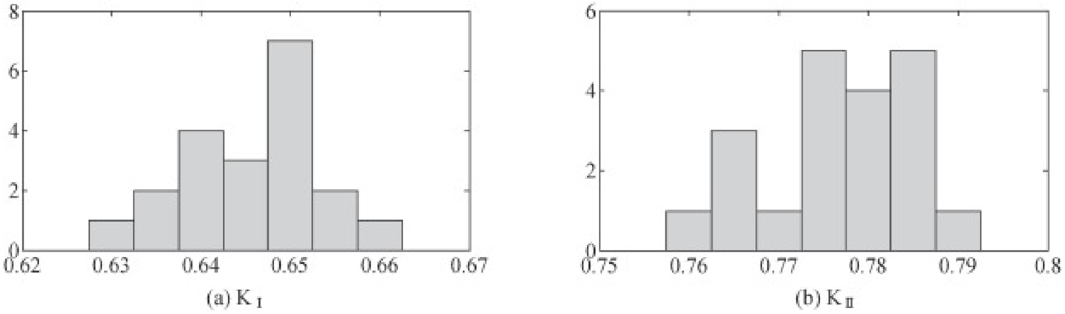

Figure 29: Histograms of macro crack SIF in presence of micro cracks (Liu et al., 2018)

After concluding that the micro cracks nearest the macro crack tip provide the most influence, the case study investigates the effect of micro crack orientation relative the macro crack. A single, static micro crack is arranged near the macro crack tip, and the inclination angle of the micro crack relative to the macro crack is varied. For each inclination angle a crack growth simulation is performed. Figure 9 shows a sketch of the micro crack inclination study problem.

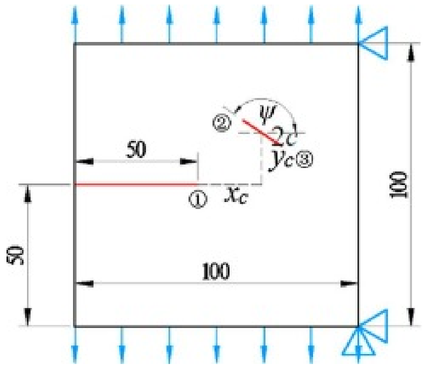

Figure 30: Micro crack inclination investigation sketch (Liu et al., 2018)

The results of the crack growth simulations indicate that the inclination angle of the micro crack relative to the macro crack effects the macro crack direction. As the inclination angle of the micro crack approaches parallel to the macro crack, the macro crack changes direction growing toward the micro crack. However, as the micro crack inclination angle approaches an angle normal to the macro crack, the effect on the macro crack growth direction is small. The crack growth paths of macro cracks in the presence of micro cracks of various inclination angles is shown in Figure 10.

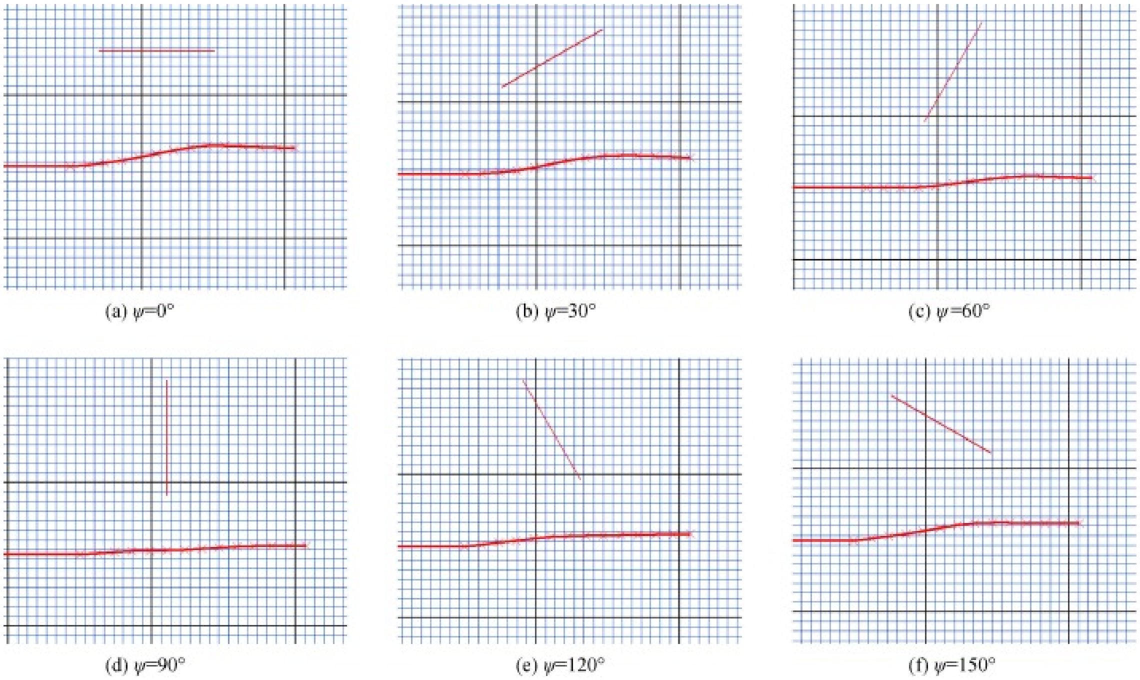
(a) ψ=0° (b) ψ=30° (c) ψ=60°

(d) ψ=90° (e) ψ=120° (f) ψ=150°

Figure 31: Macro crack growth in the presence of micro crack at various inclination angles (Liu et al., 2018)

The investigation also concludes that the micro crack inclination angle relative to the macro crack effect the macro crack growth rate. For all cases, the presence of the micro crack increases the macro crack propagation rate as shown in Figure 11.

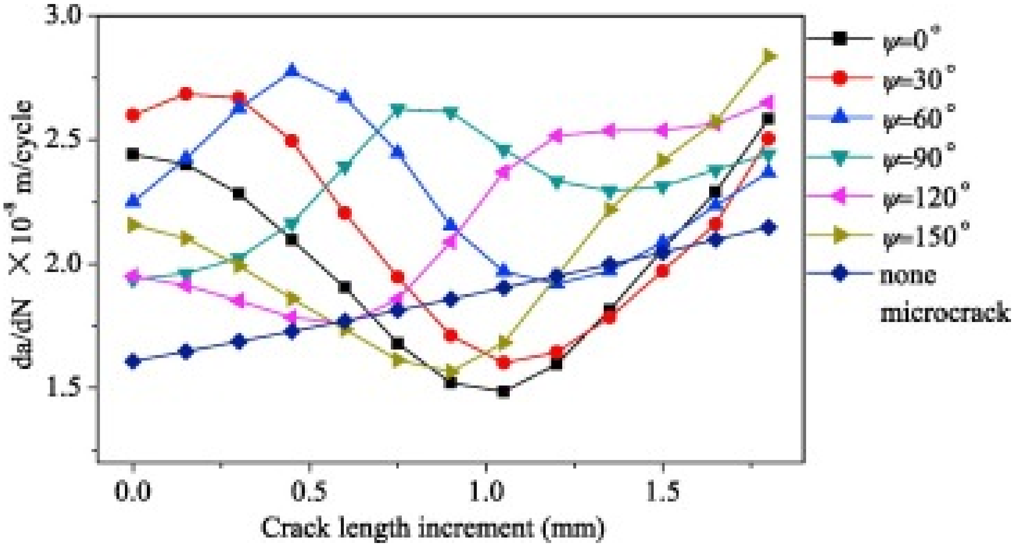

Figure 32: Variation in macro crack propagation rate with micro crack inclination angle (Liu et al., 2018)

The effect of a micro pore on macro crack propagation is investigated next. The numerical experiment considers a micro pore oriented ahead of a macro crack as shown in Figure 12.

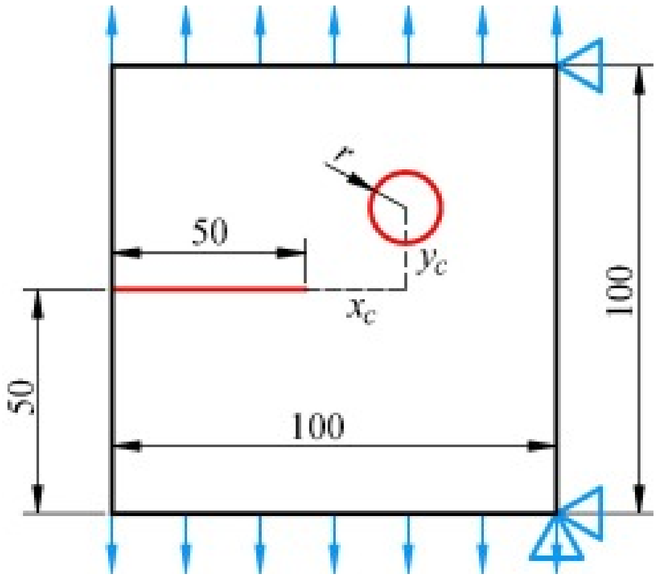

Figure 33: Sketch of micro void in the presence of a macro crack (Liu et al., 2018)

The case study considers two pore sizes and the results are compared. Both micro pores effect the crack path such that the crack propagates towards the micro pore, however, the larger pore results in a greater attraction of the macro crack as show in Figure 13.

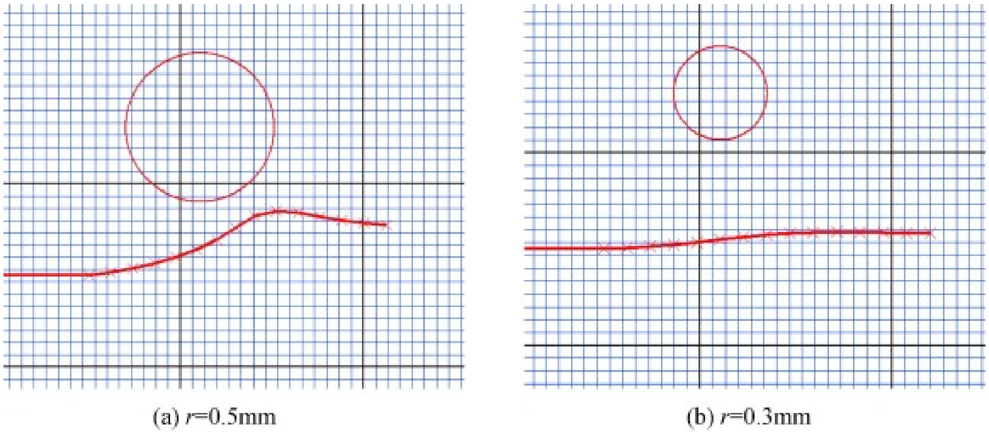

Figure 34: Effect of micro pore on macro crack path(Liu et al., 2018)

For both the micro crack and micro pore investigations, the macro crack returns to a path parallel to the original macro crack path after passing the micro defect. The case study indicates that pore size also effects macro crack propagation rates differently. Figure 14 shows the variation in macro crack propagation rate for the two micro pores considered in the study.

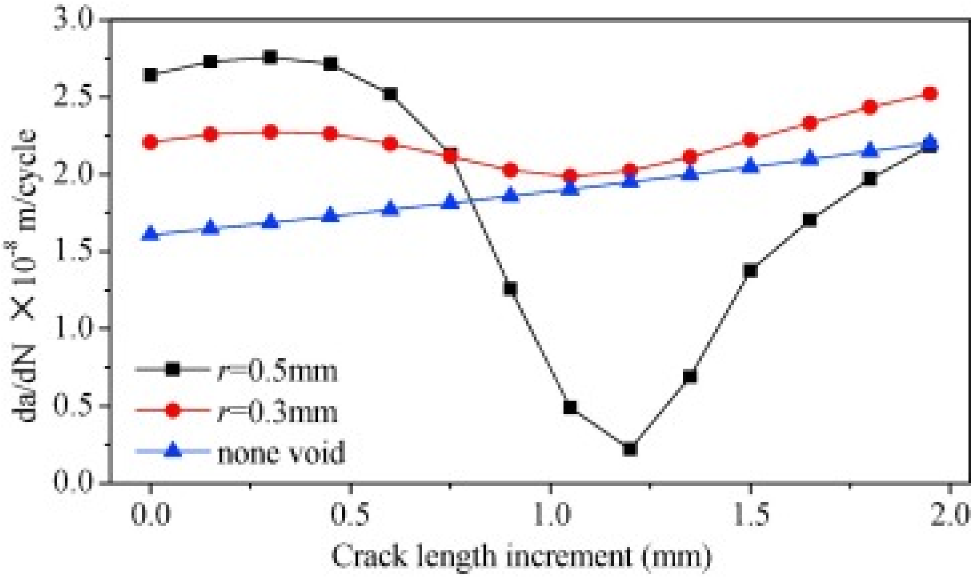

Figure 35: Macro crack propagation rates for varying micro pore sizes (Liu et al., 2018)

The effect of the larger micro pore varies as the crack length increment increases, first increasing the propagation rate, and then reducing the propagation rate. The smaller micro pore, however, tends to result in an increase in propagation rate throughout the numerical study. The case study concludes that when the ratio of the pore radius to the y-direction distance from the macro crack (see y_c in Figure 12) is relatively large that the micro pore can have a shielding effect on the macro crack, and that if the ratio is relatively small then an amplification effect is seen.

The case study investigates the effect of micro defects on the macro crack propagation using the multiscale projection method and XFEM. Both the effects of micro cracks and micro pores on the crack growth propagation of macro cracks are considered. The major conclusions of the case study are as follows:

a) Both micro crack and micro pores have an attracting effect on the macro crack path. The macro crack path will tend to move towards the defect and then return to a path parallel to the original macro crack path.
b) Micro crack SIFs are amplified by the approaching macro crack meaning that macro crack can result in increase propagation of the micro crack.
c) Micro cracks increase the propagation rate of macro cracks when the macro crack tip is near the micro crack.
d) Micro pores effect the macro crack propagation rate based on the ratio of the pore radius to the y-direction distance from the crack path. Larger ratios can produce a shielding effect on the macro crack, whereas smaller ratios can amplify the propagation rate.

CRITICAL ANALYSIS

Structural analysis methods including those concerned with static strength, durability, and damage tolerance must be developed in order to facilitate metal additive manufacturing as a common manufacturing method of aerospace structural parts. Furthermore, those methods must meet regulatory and certification requirements. Analysis of the case study presented is made from the perspective of aerospace structural analysis.

The case study presents the multiscale projection method in conjunction with XFEM to determine the effect of micro defects on macro crack propagation. The multiscale projection method allows separation of the problem into two problems: one problem at the macro scale, and one problem at the micro scale. This is advantageous in that the macro scale problem does not discretely model the micro scale defects saving both complex meshing time and long solution times that would other wise result from models with large numbers of degrees of freedom. The problem is iterative such that the macro scale problem is solved, and results are input to the micro scale problem. The micro scale problem is then solved with results of the micro scale problem input to the macro scale problem, and the process repeats until the solution converges. Iterative solutions lend themselves to automation which is an advantage to the aerospace structural analyst. The case study, unfortunately, does not provide details of the XFEM solvers or software used to automate the passing of data at the boundary between macro scale model and micro scale model. In order to facilitate industrial analysis of aerospace structure, implementation of the multiscale projection method using commercial software packages would be an advantage. The commercial finite element analysis software, ABAQUS, implements the

XFEM method and provides submodeling capabilities that allow the user to study a local, refined portion of a larger, coarse mesh model. Furthermore, ABAQUS can be automated using the Python programming language. It appears that ABAQUS has the necessary capabilities to implement the multiscale projection method as presented in the case study.

Both micro defects presented in the case study are applicable to the study of porosity in metal AM parts. The micro crack case is analogous to a lack of fusion pore, and the micro pore case is similar to a gas induced pore. A lack of fusion pore is formed when the metal powder is not sufficiently melted during the powder bed fusion process. Lack of fusion pores may only be a few print layers thick, and that thickness is much less than the characteristic length of the pore. The geometry of the lack of fusion pore can, therefore, be modeled using the micro crack approach as presented in the case study. Gas induced pores are spherical pores that develop when process or released gasses are captured in the molten metal. The micro pore (void) presented in the case study provides an excellent model of gas induced pores.

The case study conducts the numerical experiments in two dimensions (2D). Unit thickness is assumed for 2D analyses, however, the experiments are conducted at two length scales. Since the effect of micro defect on macro crack growth is considered, the macro scale thickness is the thickness that must be assumed at both scales. A consequence of the change in scale implies that the micro defects are through thickness at the macro scale meaning a micro crack extends through the macro thickness, and a micro pore extends as a cylinder through the macro thickness as shown in Figure 36.

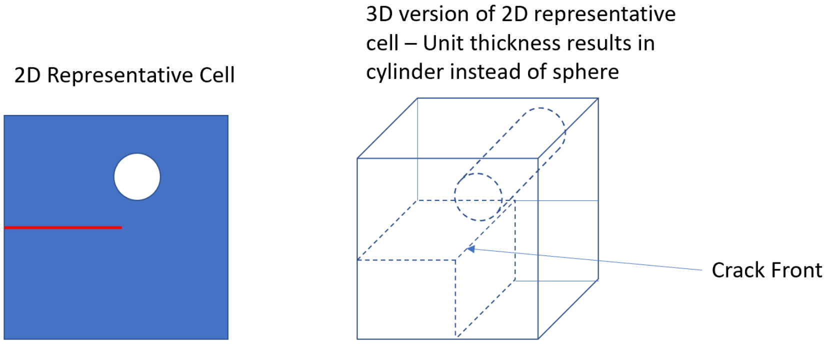

Figure 36: Unit thickness extension of 2D circular defect to 3D cylindrical defect

Obviously, the defects of interest are not accurately modeled in 2D analysis space due to the difference in length scales. It is, therefore, possible that the results presented in the case study are not accurate for the macro crack. The micro scale model must include the macro scale thickness meaning that the effects of micro defects on a macro crack must be modeled in 3D. A 3D analysis of the micro scale region requires characterization of defect distribution through the macro thickness.

RESEARCH PROPOSAL

Expanding on the work presented by Liu et. al., a similar numerical investigation of 2D circular voids and 3D spherical voids is proposed. Circular/spherical voids are reasonable models of gas porosity in metal AM parts. Numerical experiments will be conducted using Abaqus implementation of XFEM. An edge cracked plate model as shown in Figure 36 shall be considered.

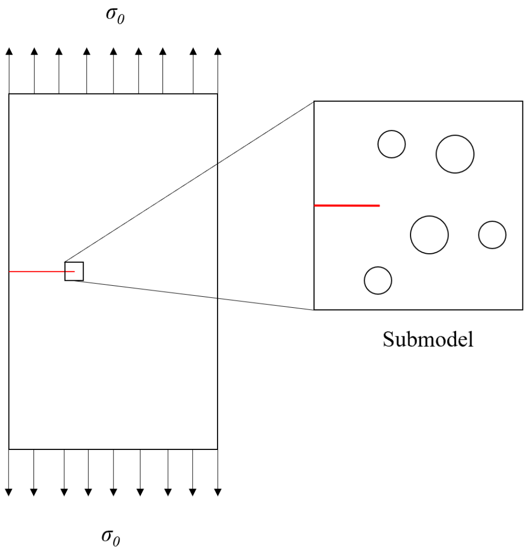

Figure 37: Edge crack plate model with submodel region shown

The Abaqus submodeling technique will be used such that the main model contains the macro crack but does not contain discrete defects. The circular/spherical defects will be discretely modeled in the submodel. Results of the 2D experiments will be compared to results from Liu et. al. 3D results will be compared to 2D results to understand the limitations of 2D representations of 3D spherical voids. There is additional interest in determining the volume fraction at which spherical voids have significant impact on the macro crack growth. If possible, a 3D representation of porosity in a test specimen will be modeled and results compared to experimental data.

Submodeling in Abaqus allows the user to study in detail a region of interest in a larger, global model. In most cases the region of interest uses a finer, more detailed mesh. Submodeling is Abaqus also allows for the submodel to be modeled using 3D elements even when the global model is modeled using 2D shell elements know as ‘shell-to-solid’ submodeling. Submodeling involves a two step process where the global model is created and analyzed, then a submodel is created. The boundaries of the submodel are driven with time-dependent variables saved during analysis of the global model. (Systems, 2018)

The first numerical experiment will be a recreation of the circular 2D void experiment conducted by Liu et. al. as shown in Figure 33 except using submodeling in Abaqus. The experiment will be conducted using 2D shell elements for both the global model and the submodel just as Liu et. al. The purpose of this experiment is to establish a control. The next numerical experiment will extend the first experiment utilizing the ‘shell-to-solid’ submodeling technique. The global model will use 2D shell elements, however, the submodel will use 3D elements to characterize the domain around the macro crack tip. Several submodels will be studied including the extension of the 2D circle to a 3D cylinder through the thickness, a single spherical void, and multiple spherical voids as shown in Figure 38. The purpose of this experiment is to study the effect of 2D representations of 3D defects relative to 3D representation of 3D defects.

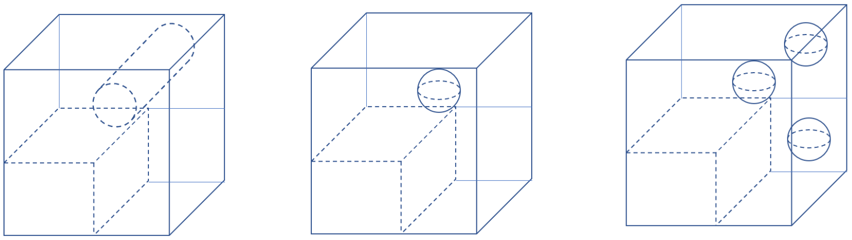

Figure 38: Sketches of 3D submodels for study

The next numerical experiments will extend both the global model and the submodel to 3D elements. The same submodel configurations used in the 'shell-to-solid' experiment will be used here. The purpose of this experiment is to determine the sensitivity of results to through thickness boundary conditions derived from 2D global model versus those boundary conditions derived from 3D global model. Finally, if test specimen data is available, a 3D global/submodel of the test specimen will be considered and results compared to experimental data.

REFERENCES

Bandyopadhyay, A., & Traxel, K. D. (2018). Invited review article: Metal-additive manufacturing—Modeling strategies for application-optimized designs. *Additive Manufacturing, 22*, 758-774. doi:10.1016/j.addma.2018.06.024

Belytschko, T., Liu, W. K., Moran, B., & Elkhodary, K. I. (2014). *Nonlinear Finite Elements for Continua and Structures* (Second edition ed.). Chichester, West Sussex, UK : Hoboken, New Jersey: Wiley.

DebRoy, T., Wei, H. L., Zuback, J. S., Mukherjee, T., Elmer, J. W., Milewski, J. O., . . . Zhang, W. (2018). Additive manufacturing of metallic components – Process, structure and properties. *Progress in Materials Science, 92*, 112-224. doi:10.1016/j.pmatsci.2017.10.001

Domfang Ngnekou, J. N., Nadot, Y., Henaff, G., Nicolai, J., Kan, W. H., Cairney, J. M., & Ridosz, L. (2019). Fatigue properties of AlSi10Mg produced by Additive Layer Manufacturing. *International Journal of Fatigue, 119*, 160-172. doi:https://doi.org/10.1016/j.ijfatigue.2018.09.029

Galy, C., Le Guen, E., Lacoste, E., & Arvieu, C. (2018). Main defects observed in aluminum alloy parts produced by SLM: From causes to consequences. *Additive Manufacturing, 22*, 165-175. doi:https://doi.org/10.1016/j.addma.2018.05.005

Kumar, S., Singh, I. V., & Mishra, B. K. (2015). A homogenized XFEM approach to simulate fatigue crack growth problems. *Computers & Structures, 150*, 1-22. doi:https://doi.org/10.1016/j.compstruc.2014.12.008

Li, H., Li, J., & Yuan, H. (2018). A review of the extended finite element method on macrocrack and microcrack growth simulations. *Theoretical and Applied Fracture Mechanics, 97*, 236-249. doi:https://doi.org/10.1016/j.tafmec.2018.08.008

Liu, G., Zhou, D., Guo, J., Bao, Y., Han, Z., & Lu, J. (2018). Numerical simulation of fatigue crack propagation interacting with micro-defects using multiscale XFEM. *International Journal of Fatigue, 109*, 70-82. doi:https://doi.org/10.1016/j.ijfatigue.2017.12.012

Loehnert, S., & Belytschko, T. (2007). A multiscale projection method for macro/microcrack simulations. *International Journal for Numerical Methods in Engineering, 71*(12), 1466-1482. doi:10.1002/nme.2001

Mohammadi, S. (2008). *Extended finite element method for fracture analysis of structures*: Oxford ; Malden, MA : Blackwell Pub., 2008.

Molaei, R., & Fatemi, A. (2018). Fatigue Design with Additive Manufactured Metals: Issues to Consider and Perspective for Future Research. *Procedia Engineering, 213*, 5-16. doi:https://doi.org/10.1016/j.proeng.2018.02.002

Ngo, T. D., Kashani, A., Imbalzano, G., Nguyen, K. T. Q., & Hui, D. (2018). Additive manufacturing (3D printing): A review of materials, methods, applications and challenges. *Composites Part B: Engineering, 143*, 172-196. doi:10.1016/j.compositesb.2018.02.012

Romero, C., Yang, F., & Bolzoni, L. (2018). Fatigue and fracture properties of Ti alloys from powder-based processes – A review. *International Journal of Fatigue, 117*, 407-419. doi:https://doi.org/10.1016/j.ijfatigue.2018.08.029

Seifi, M., Salem, A., Satko, D., Shaffer, J., & Lewandowski, J. J. (2017). Defect distribution and microstructure heterogeneity effects on fracture resistance and fatigue behavior of EBM

Ti–6Al–4V. *International Journal of Fatigue, 94*, 263-287. doi:https://doi.org/10.1016/j.ijfatigue.2016.06.001

Systems, D. (Producer). (2018). Simula Online User Assitance 2018.

Zhai, Y., Galarraga, H., & Lados, D. A. (2016). Microstructure, static properties, and fatigue crack growth mechanisms in Ti-6Al-4V fabricated by additive manufacturing: LENS and EBM. *Engineering Failure Analysis, 69*, 3-14. doi:https://doi.org/10.1016/j.engfailanal.2016.05.036

Zhang, J., Song, B., Wei, Q., Bourell, D., & Shi, Y. (2018). A review of selective laser melting of aluminum alloys: Processing, microstructure, property and developing trends. *Journal of Materials Science & Technology*. doi:https://doi.org/10.1016/j.jmst.2018.09.004

Zhang, Y., Wu, L., Guo, X., Kane, S., Deng, Y., Jung, Y. G., . . . Zhang, J. (2018). Additive Manufacturing of Metallic Materials: A Review. *Journal of Materials Engineering and Performance, 27*(1). doi:10.1007/s11665-017-2747-y